remote sensing

MDPI

Article

Assessing the Future ODYSEA Satellite Mission for the Estimation of Ocean Surface Currents, Wind Stress, Energy Fluxes, and the Mechanical Coupling Between the Ocean and the Atmosphere

Marco Larrañaga [1,2,*], Lionel Renault [2], Alexander Wineteer [3], Marcela Contreras [4], Brian K. Arbic [5], Mark A. Bourassa [1,6] and Ernesto Rodriguez [3]

1 Center for Ocean-Atmospheric Prediction Studies (COAPS), Florida State University, Tallahassee, FL 32306, USA; mbourassa@coaps.fsu.edu
2 LEGOS, Université de Toulouse, CNES-CNRS-IRD-UPS, 14 Avenue Edouard Belin, 31400 Toulouse, France; lionel.renault@ird.fr
3 Jet Propulsion Laboratory, California Institute of Technology, Pasadena, CA 91109, USA; wineteer@jpl.nasa.gov (A.W.); ernesto.rodriguez@jpl.nasa.gov (E.R.)
4 Institut des Géosciences de l'Environnement, University Grenoble Alpes, CNRS, IRD, Grenoble INP, INRAE, IGE, 38000 Grenoble, France; marcela.contreras@univ-grenoble-alpes.fr
5 Department of Earth and Environmental Sciences, University of Michigan, Ann Arbor, MI 48109, USA; arbic@umich.edu
6 Department of Earth, Ocean and Atmospheric Science, Florida State University, Tallahassee, FL 32306, USA
* Correspondence: marco.larranaga@fsu.edu

Abstract: Over the past decade, several studies based on coupled ocean–atmosphere simulations have shown that the oceanic surface current feedback to the atmosphere (CFB) leads to a slow-down of the mean oceanic circulation and, overall, to the so-called eddy killing effect, i.e., a sink of kinetic energy from oceanic eddies to the atmosphere that damps the oceanic mesoscale activity by about 30%, with upscaling effects on large-scale currents. Despite significant improvements in the representation of western boundary currents and mesoscale eddies in numerical models, some discrepancies remain when comparing numerical simulations with satellite observations. These discrepancies include a stronger wind and wind stress response to surface currents and a larger air–sea kinetic energy flux from the ocean to the atmosphere in numerical simulations. However, altimetric gridded products are known to largely underestimate mesoscale activity, and the satellite observations operate at different spatial and temporal resolutions and do not simultaneously measure surface currents and wind stress, leading to large uncertainties in air–sea mechanical energy flux estimates. ODYSEA is a new satellite mission project that aims to simultaneously monitor total surface currents and wind stress with a spatial sampling interval of 5 km and 90% daily global coverage. This study evaluates the potential of ODYSEA to measure surface winds, currents, energy fluxes, and ocean–atmosphere coupling coefficients. To this end, we generated synthetic ODYSEA data from a high-resolution coupled ocean–wave–atmosphere simulation of the Gulf Stream using ODYSIM, the Doppler scatterometer simulator for ODYSEA. Our results indicate that ODYSEA would significantly improve the monitoring of eddy kinetic energy, the kinetic energy cascade, and air–sea kinetic energy flux in the Gulf Stream region. Despite the improvement over the current measurements, the estimates of the coupling coefficients between surface currents and wind stress may still have large uncertainties due to the noise inherent in ODYSEA, and also due to measurement capabilities related to wind stress. This study evidences that halving the measurement noise in surface currents would lead to a more accurate estimation of the surface eddy kinetic energy and wind stress coupling coefficients. Since measurement

check for updates

Academic Editor: Biao Zhang

Received: 8 November 2024
Revised: 21 December 2024
Accepted: 27 December 2024
Published: 16 January 2025

Citation: Larrañaga, M.; Renault, L.; Wineteer, A.; Contreras, M.; Arbic, B.K.; Bourassa, M.A.; Rodriguez, E. Assessing the Future ODYSEA Satellite Mission for the Estimation of Ocean Surface Currents, Wind Stress, Energy Fluxes, and the Mechanical Coupling Between the Ocean and the Atmosphere. *Remote Sens.* **2025**, *17*, 302. https://doi.org/10.3390/rs17020302

Copyright: © 2025 by the authors. Licensee MDPI, Basel, Switzerland. This article is an open access article distributed under the terms and conditions of the Creative Commons Attribution (CC BY) license (https://creativecommons.org/licenses/by/4.0/).

noise in surface currents strongly depends on the square root of the transmit power of the Doppler scatterometer antenna, noise levels can be reduced by increasing the antenna length. However, exploring other alternatives, such as the use of neural networks, could also be a promising approach. Additionally, the combination of wind stress estimation from ODYSEA with other satellite products and numerical simulations could improve the representation of wind stress in gridded products. Future efforts should focus on the assessment of the potential of ODYSEA in quantifying the production of eddy kinetic energy through horizontal energy fluxes and air–sea energy fluxes related to divergent and rotational motions.

Keywords: ODYSEA; Doppler scatterometer; surface currents; wind stress; eddy kinetic energy; horizontal energy fluxes; wind work; coupling coefficients

1. Introduction

In the last couple of decades, thanks to advances in numerical modeling and satellite observations, mesoscale air–sea interactions have received growing interest from the scientific community. In particular, the current feedback to the atmosphere (CFB; [1–5]), which is essentially the influence of surface currents on the overlying atmosphere, has been shown to be a missing piece in ocean modeling. CFB has been shown to slow down the mean oceanic circulation [6,7] and, overall, to induce the so-called eddy killing effect, i.e., a sink of kinetic energy from oceanic eddies to the atmosphere that damps the oceanic mesoscale activity by about 30% [5,8–10]. The sink of kinetic energy caused by CFB arises from the interaction between surface currents, winds, and wind stress. A positive (negative) current anomaly induces a negative (positive) wind stress anomaly, which modifies the resistance at the surface and allows for the re-energization of winds and, consequently, the ocean. Therefore, a negative (positive) wind stress anomaly results in a positive (negative) wind anomaly. As positive wind stress anomalies are more prevalent, the transfer of energy from surface currents to the atmosphere is mainly driven by wind stress anomalies, while the partial re-energization of the ocean is attributed to the wind anomalies [5]. The damping of the oceanic mesoscale activity further leads to a weakening of the eddy–mean flow interaction (the inverse cascade of kinetic energy), stabilizing and improving the representation of emblematic western boundary currents such as the Gulf Stream, the Agulhas Current, and the Loop Current [7,11–15]. Furthermore, the current feedback promotes the occurrence of mesoscale eddies with more realistic properties (e.g., thermohaline characteristics, energy levels, and lifetime) and trajectories by modifying their detachment location, periodicity, and interactions with the atmosphere [5,15].

As a measure of the eddy killing effect, the wind work has been broadly used to investigate the extent to which CFB modulates the intensity of wind-driven currents, i.e., Ekman currents, near-inertial oscillations, and internal gravity waves, as well as (sub)mesoscale and large-scale currents [5,9,15–20]. CFB efficiency can also be characterized by means of the coupling coefficient s_τ, which is defined as the slope of the linear regression between mesoscale surface current vorticity and wind stress curl. The more negative the s_τ, the more efficient the eddy killing.

However, despite significant improvements in ocean dynamics in numerical models, discrepancies remain when coupled numerical simulations are compared with satellite observations. Coupled ocean–atmosphere simulations exhibit a stronger wind stress response to CFB, a larger eddy wind work, and, consistently, a more negative s_τ coupling coefficient compared to those estimated from the combination of surface currents derived from alti-

metric measurements [21] and wind stress estimations derived from scatterometers [22] (see [7,8,23]). While there is no doubt that some of these discrepancies are due to model bias, the current satellite products have large systematic errors and important sampling differences. Gridded altimetric products specifically, which rely on the geostrophic balance to estimate surface currents, largely underestimate the mesoscale levels of energy and can only resolve mesoscale eddies with a diameter larger than 100 km [24–27]. In addition, satellite observations operate at different spatial and temporal resolutions and do not simultaneously measure surface currents and wind stress, which is critical for accurate quantification of kinetic energy flux between the ocean and the atmosphere (the wind work) and the s_τ coupling coefficient [8,28]. Finally, because scatterometers provide winds relative to oceanic currents, they cannot adequately characterize the CFB wind response.

The Ocean Dynamics and Sea Exchanges with the Atmosphere (ODYSEA) satellite project, which includes a pencil-beam Doppler scatterometer, would allow us to simultaneously measure total surface currents and winds with a spatial resolution of 5 km, temporal resolution of 12 h, and global coverage within 1–2 days. Surface current radial velocities will be measured from the Doppler shift of the backscattered signal, which is proportional to the surface current speed component along the line of sight. Therefore, the computation of surface currents will be achieved by observing radial velocities along different azimuth angles [29]. The Ka-band Doppler scatterometer will allow ODYSEA to estimate ocean surface equivalent neutral winds, improving by a factor of around 3 the spatial resolution with respect to estimations from a Ku-band scatterometer [29,30]. Measurement noise follows Gaussian distributions with standard deviations of 50 cm s^{-1} for currents in low-wind conditions and 1 m s^{-1} for winds [28,30,31]. A previous study [28] analyzed the ODYSEA's capability in estimating wind work and its sensitivity to measurement uncertainties. The authors used a measurement simulator fed by results from a 4 km ocean–atmosphere coupled simulation to show that ODYSEA sampling would properly represent the wind work, even if surface current errors reach 1 m s^{-1}.

This study aims to go one step further by assessing how well ODYSEA could measure surface winds, currents, energy fluxes, and ocean–atmosphere coupling coefficients. It mainly focuses on the consequences of uncertainties, including (i) those associated with measurement capabilities related to sub-sampling, as well as (ii) noise related to the performance of traditional pencil-beam scatterometers, and proposes strategies to address them. To this end, we generate synthetic ODYSEA data from a coupled ocean–surface waves–atmosphere high-resolution numerical simulation of the Gulf Stream and using the Doppler scatterometer simulator ODYSIM (https://github.com/awineteer/odysea-science-simulator; accessed on 10 June 2023). Our study focuses on the Gulf Stream region, which is characterized by strong and large (sub)mesoscale currents but also by the occurrence of large surface gravity waves (Figure 1).

The paper is organized as follows: The models, ODYSEA simulator, and datasets used in this work are described in Section 2. Section 3 demonstrates the capabilities of ODYSEA in reproducing the ocean surface kinetic energy and wind stress, as well as kinetic energy cascades, air–sea energy fluxes related to wind work, and ocean–atmosphere coupling coefficients. This section also analyzes the consequences of measurement uncertainties, e.g., sub-sampling and noise, and proposes strategies for dealing with them. Finally, the results are discussed in Section 4.

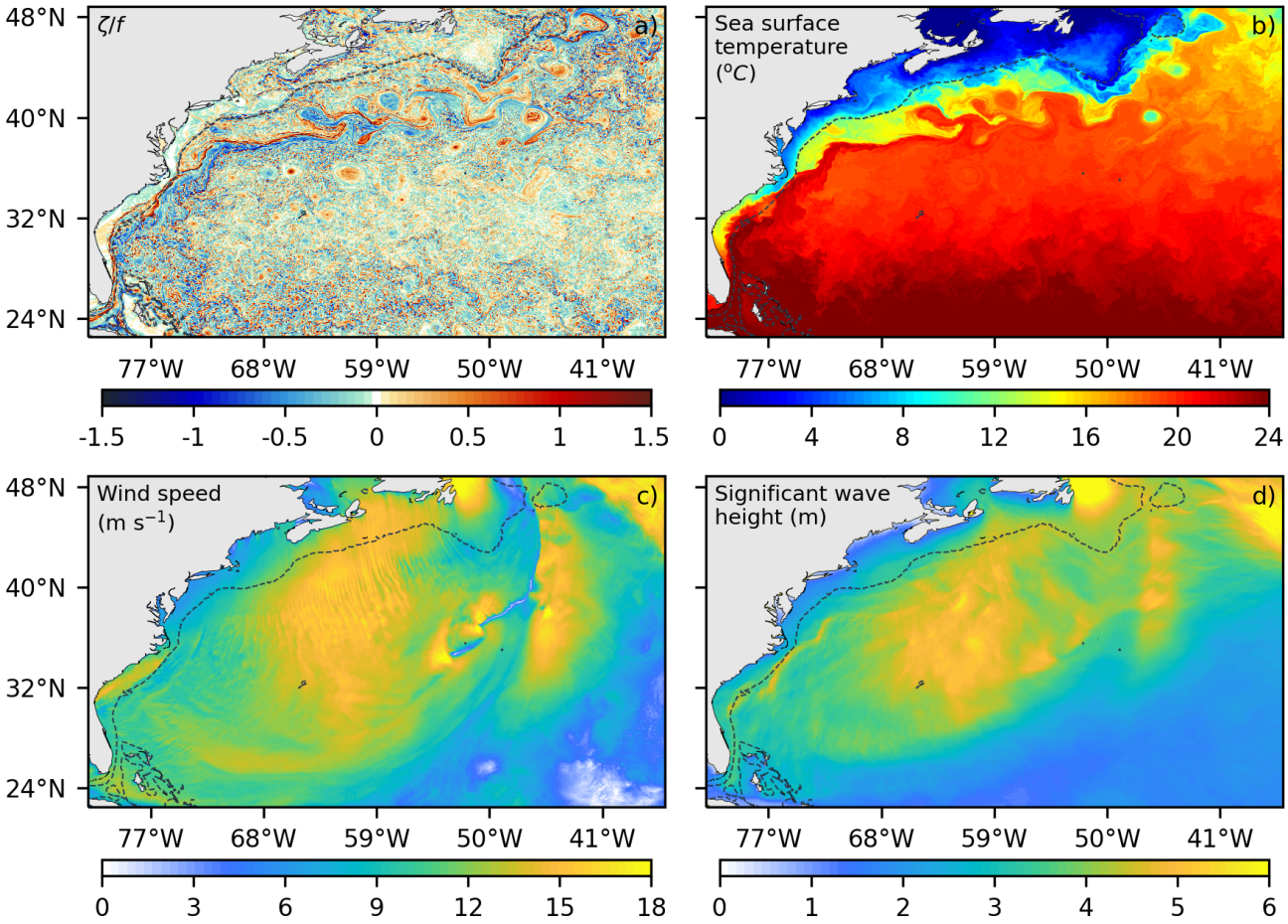

Figure 1. Snapshots of relative vorticity (**a**) (normalized by the planetary vorticity f), sea surface temperature (**b**), wind speed (**c**), and significant wave height (**d**) from the CROCO-WRF-WWIII coupled system results for 29 January 2005. The black segmented line represents the 500 m depth contour.

2. Methods and Data

2.1. ODYSIM

ODYSIM is a Doppler scatterometer simulator designed to explore the capabilities of ODYSEA. It generates synthetic ODYSEA data from numerical simulations to assess the measurement of surface currents and winds [28,30]. The simulator is configured with the following specifications: a satellite with a 5.0 × 0.35 m antenna, 400 W transmit power, a 590 km sun-synchronous polar orbit with a 4-day repeat cycle, and an incidence angle of 56°. This configuration allows a wide measurement swath of about 1700 km with a daily global coverage of around 90% and a spatial resolution of 5 km for surface currents and winds [28,30,31].

In addition to providing synthetic data, ODYSIM also allows for assessing the potential consequences of inherent uncertainties in the measurements because it includes a parametrization of random errors or noise, which largely depend on the wind speed and the look geometry [29,30]. This measurement noise primarily reflects the retrieval uncertainties typical of pencil-beam scatterometers and does not account for additional noise sources, such as those associated with rainfall, sea surface temperature, or sea state [30–34]. The commonly referenced performance baseline noise for ODYSEA is stated to be 50 cm s^{-1} for surface currents and 1 m s^{-1} for surface winds for a spatial sampling interval of 5 km [31]. However, Ref. [30] demonstrated that noise associated with surface current measurements can be significantly higher at the center and edges of the swath while it diminishes over the "sweet spots", which are the regions between the center and the edges.

It is important to consider that the ODYSEA synthetic data, which depend on the ODYSIM configuration and the parametrized noise, are also largely influenced by the numerical simulation used as an input to the ODYSIM. While comparisons between ODYSIM results from different simulations are valid, they must be interpreted with consideration of the specific model configurations and the fundamental assumptions of each simulation.

In this study, ODYSIM generates synthetic ODYSEA measurements by extracting surface currents and wind stress data from high-spatial-resolution coupled ocean–atmosphere–wave simulations performed over the Gulf Stream region. The details of the configuration are provided below.

2.2. Coupled Ocean–Surface Waves–Atmosphere Numerical Simulation

The coupled ocean–atmosphere–wave system uses the Coastal and Regional Ocean Community (CROCO) version of the Ocean Modeling System (ROMS) model [35,36] to reproduce the ocean dynamics at a spatial resolution of $1/42^\circ$ ($\sim$2.2 km), the Weather Research and Forecast (WRF) model [37] to reproduce the atmosphere dynamics with a spatial resolution of $1/15^\circ$ ($\sim$6 km), and the WaveWatch III (WW3) surface gravity wave models to simulate sea state with a spatial resolution of $\sim$6 km. The domains for CROCO, WRF, and WW3 are illustrated in Figure 1a. The numerical models and configurations are similar to the ones employed in [38,39], and the following model descriptions are derived from those references with minor modifications. Briefly, the simulations are in good agreement with observations, as shown by [18,38,39], and reproduce a stable path of the Gulf Stream with intense surrounding mesoscale activity, realistic atmospheric low-level circulation and heat fluxes, and a fair representation of the surface gravity waves.

2.2.1. The CROCO Configuration

The CROCO model is a terrain-following, free-surface Boussinesq model that uses a split-explicit time-stepping scheme. While it is available in both hydrostatic and non-hydrostatic versions, we use the hydrostatic version in this study.

Fifth-order upstream biased momentum advection is used [40,41], which reduces the numerical dispersion and diffusion and allows the achievement of an effective resolution of about 10 km (about 5 times the horizontal resolution). For horizontal tracer transport, the model employs a rotated split third-order upstream scheme for discretization. Notably, the diffusive component of this scheme is rotated along isopycnal surfaces, a method aimed at minimizing excessive diapycnal mixing, as suggested by [42–44]. To represent turbulent diffusion processes at the surface, bottom, and interior of the ocean, K-Profile Parameterization (KPP; Ref. [44]) is used.

As depicted in Figure 1, the CROCO model is implemented over the north-west Atlantic Ocean with a horizontal spatial sampling interval of $1/42^\circ$ ($\sim$2.2 km). It extends from 22.5°N to 48.84°N and from 36°W to 82°W. The full configuration is described in [38] as the "TD" simulation, i.e., a simulation that is forced at its lateral boundary by the $1/12^\circ$ daily mean Mercator Glorys12V1 product [45], and by barotropic tides (height and currents) from the global tidal model TPXOv.7 [46]. Bottom drag is quadratic and parameterized through a logarithmic law of the wall with a roughness length of $z_0 = 10^{-2}$ m. The coupled simulation runs for 1 year, starting on 1 January 2005, after a spin-up of 5 years (see [18] for more details).

2.2.2. The Weather Research and Forecast Model Configuration

WRF 4.2 [37] is implemented over a slightly larger domain to avoid issues related to the sponge layer of the WRF. It has a horizontal spatial sampling interval of approximately 6.2 km [39] and uses 50 hybrid levels with a model top pressure set at 1000 Pa and a first level at 10 m over the ocean. The model is initialized and forced at its lateral boundary

by the ERA5 dataset [47], which is a fifth-generation reanalysis dataset produced by the European Centre for Medium-Range Weather Forecasts (ECMWF).

We use the following set of parameterizations: the KIAPS SAS (KSAS; Korean Institute of Atmospheric Prediction Systems Simplified Arakawa–Schubert) convective scheme [48,49], the WRF Single-Moment 6-Class (WSM6) Microphysics Scheme with droplet concentration inclusion [50,51], the Dudhia shortwave radiation scheme [52], the Rapid Radiative Transfer Model Longwave Radiation Scheme [53], the Yonsei University (YSU) Planetary Boundary Layer Scheme [54], the Revised MM5 Surface Layer Scheme [55], and the Noah Land Surface Model [56]. The current feedback parameterization is implemented in both the surface layer and planetary boundary layer schemes following the approach of [57].

2.2.3. The WaveWatch III Model Configuration

WW3 solves the random-phase spectral action density balance equation for specific wavenumber–direction spectra, encompassing various physical processes. These include wind–wave interactions, nonlinear wave–wave interactions, wave–bottom interactions, depth-induced breaking, dissipation, and shoreline reflection, all of which are parameterized within the model. To address numerical artifacts arising from discrete directions of wave propagation, the third-order Ultimate Quickest scheme by [58], augmented with the Garden Sprinkler correction, is employed. Nonlinear wave–wave interactions are accounted for using the Discrete Interaction Approximation (DIA) method proposed by [59]. The wind–wave interaction source term introduced by [60] is integrated into the model, featuring a parameterization based on saturation-based dissipation to mitigate unrealistically large drag coefficients observed under high-wind conditions. Furthermore, depth-induced wave breaking, following the formulation by [61], and bottom friction source terms as outlined by [62] are incorporated.

The grid used in the WW3 model covers the same geographic region and has the same spatial resolution as the Weather Research and Forecasting (WRF) model. Specifically, the spectral discretization used in WW3 consists of 24 directions (at 15° intervals) and 32 frequency bins. To establish lateral boundary conditions for the coupled simulations, a stand-alone WW3 simulation is performed over the entire Atlantic region for the period from 2004 to 2006. This stand-alone simulation uses the same spectral discretization and a spatial resolution of 0.2°. The wind forcing data used in this stand-alone simulation are obtained from the Climate Forecast System Reanalysis (CFSR) dataset [63]. The derived spectra from this stand-alone WW3 run are then imposed hourly at the boundaries of WW3 in the coupled simulations.

2.2.4. Coupling Strategy

The coupling strategy is illustrated in Figure 2. The OASIS (Ocean–Atmosphere–Sea Ice–Snow model) coupler [64] is used at the interface of the models to perform the exchanges of the different fields. The following fields are exchanged hourly between the models:

- WRF sends to CROCO momentum (surface stress), heat, and freshwater flux and receives from CROCO the sea surface temperature and currents.
- WRF sends to WW3 the wind and receives the Charnock parameter from WW3.
- CROCO gives the sea surface height and the surface currents to WW3 and receives the net wave-supported stress and wave-to-ocean momentum flux, as well as the significant wave height, mean wave period, and mean wave direction used to compute the Stokes Drift.

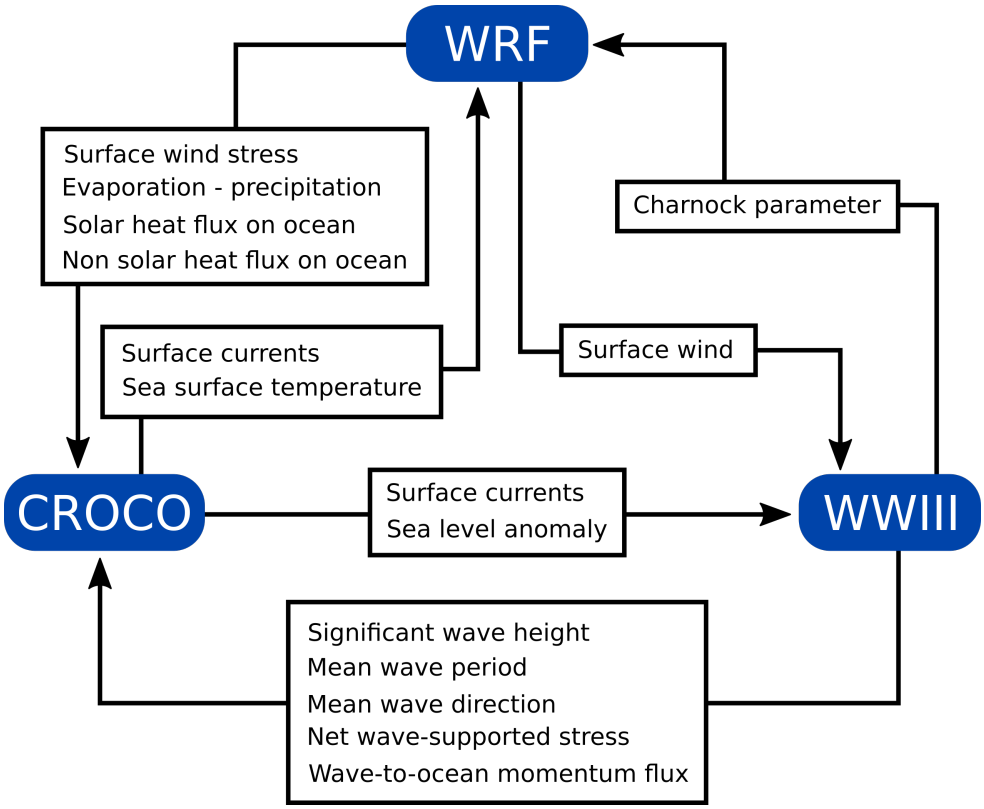

Figure 2. Coupling strategy for the CROCO-WW3-WRF system.

2.3. ODYSEA Datasets

Two main datasets are built from ODYSIM results, corresponding to along-track and gridded formats. In addition, additional datasets are generated by adding parametric measurement noise to the primary datasets and by applying spatial filters to reduce this noise. A summary of the properties of the generated datasets is shown in Table 1. To differentiate between the datasets generated from the ODYSIM simulator and the outputs of the coupled simulation, we adopt the following naming convention:

- The first three letters are "ODS", to denote that the dataset is generated by ODYSIM.
- Following "ODS", the dataset level is indicated: "L2" or "L3". "L2" represents the ODYSEA along-track data mapped onto a standardized grid with a resolution of 5 km. "L3" indicates a gridded dataset obtained by applying a running mean to the L2 products.
- The running mean applied is then specified: "1.5 day" or "3 day".
- The letter "N" indicates the consideration of the parametrized noise from ODYSIM, which is added to the along-track data. Measurement noise depends on instrument parameters, look direction, and the strength of the return signal. The signal strength is proportional to the radar cross-section, which depends on wind speed and direction through an empirically derived wind geophysical model function [29,30].
- "$N_{0.5}$" indicates the consideration of only the half value of parametrized noise.
- To mitigate measurement noise, spatial smoothing is implemented using a window of either 15 km or 25 km. In such instances, the use of a spatial filter is denoted by the prefix "F" followed by the length of the spatial filter (15 or 25 km).

In the L2 products, following [28,30], the center and edges of the swath are removed to eliminate the regions with large uncertainties. In addition, surface currents where winds are weaker than 3 m s^{-1} are removed to ensure an averaged noise of about 50 cm s^{-1} (Figure 3b). This excludes about 20% of the data (Figure 3a) but improves the representation of surface

currents. Analyzing L2 datasets allows us to quantify the uncertainties related to satellite sub-sampling. L3 datasets are necessary to compute horizontal energy fluxes and coupling coefficients between the sea surface currents and the atmosphere (see Sections 3.3 and 3.4). Therefore, comparisons from "L2" to "L3" datasets will help us assess the consequences of temporal filters in the computation of these parameters. Comparing "N" and "L" datasets will enable us to identify how parametric noise affects data values in terms of statistical properties. A comparison between "N" and "F" datasets will allow us to analyze the effectiveness of spatial filters in reducing the impact of noise in ODYSEA measurements. Finally, a comparison between "N" and "$N_{0.5}$" datasets will allow us to analyze the impact of considering only half of the parametrized noise.

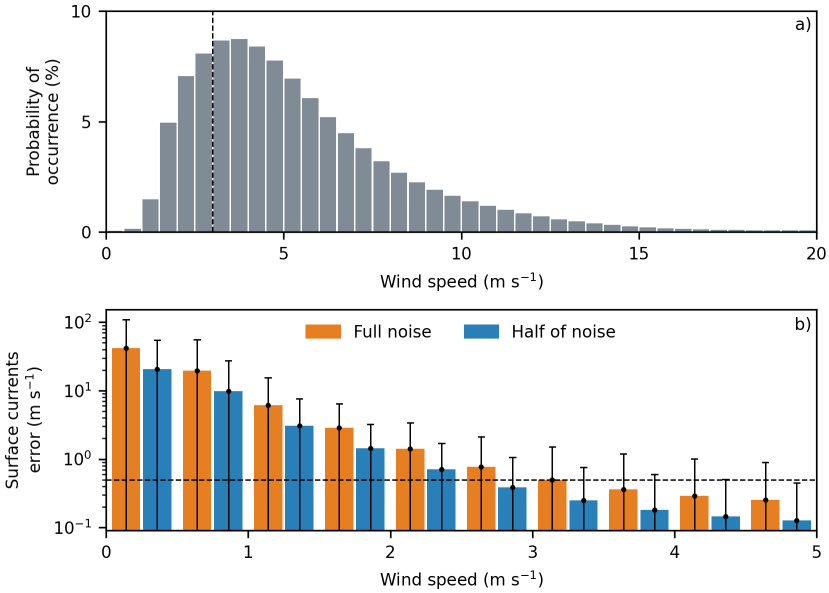

Figure 3. (**a**) Probability distribution of wind speeds. The vertical dashed line indicates the 3 m s^{-1} wind speed threshold. (**b**) Mean noise (colored bars) of surface currents and associated standard deviation (error bars) as a function of wind speed in the ODSL2N dataset. Noise statistics are derived from the magnitude of the latitudinal and longitudinal components of surface currents noise. The horizontal dashed line indicates the 50 cm s^{-1} noise threshold.

Table 1. Dataset properties: noise, temporal filters, and spatial filters.

Datasets	Noise	Temporal Filter	Spatial Filter
ODSL2	No	No	No
ODSL2N	Full	No	No
ODSL2N$_{0.5}$	Full	No	No
ODSL2NF$_{15km}$	Full	No	15 km
ODSL3$_{1.5day}$	No	1.5 days	No
ODSL3$_{1.5day}$N	Full	1.5 days	No
ODSL3$_{1.5day}$N$_{0.5}$	Half	1.5 days	No
ODSL3$_{1.5day}$NF$_{25km}$	Full	1.5 days	25 km
ODSL3$_{1.5day}$N$_{0.5}$F$_{15km}$	Half	1.5 days	15 km
ODSL3$_{3day}$	No	3 days	No
ODSL3$_{3day}$N	Full	3 days	No
ODSL3$_{3day}$N$_{0.5}$	Half	3 days	No
ODSL3$_{3day}$NF$_{25km}$	Full	3 days	25 km
ODSL3$_{3day}$N$_{0.5}$F$_{15km}$	Half	3 days	15 km

An example of the surface currents and wind stress are depicted in Figure 4. At first glance, it seems that both ODSL3$_{1.5day}$NF$_{15km}$ and ODSL3$_{3day}$NF$_{15km}$ are able to reproduce the mesoscale activity, mainly differing in the occurrence of spatial gaps related to the exclusion of the data at the center and edges of the swath in ODSL3$_{1.5day}$NF$_{15km}$ (Figure 4a,c,e). Regarding wind stress, it is evident that longer averaged periods promote an important smoothing over the fields (Figure 4b,d,f). This is associated with the propagation of fast atmosphere features, i.e., storms, that cannot be properly sampled by the satellite [28].

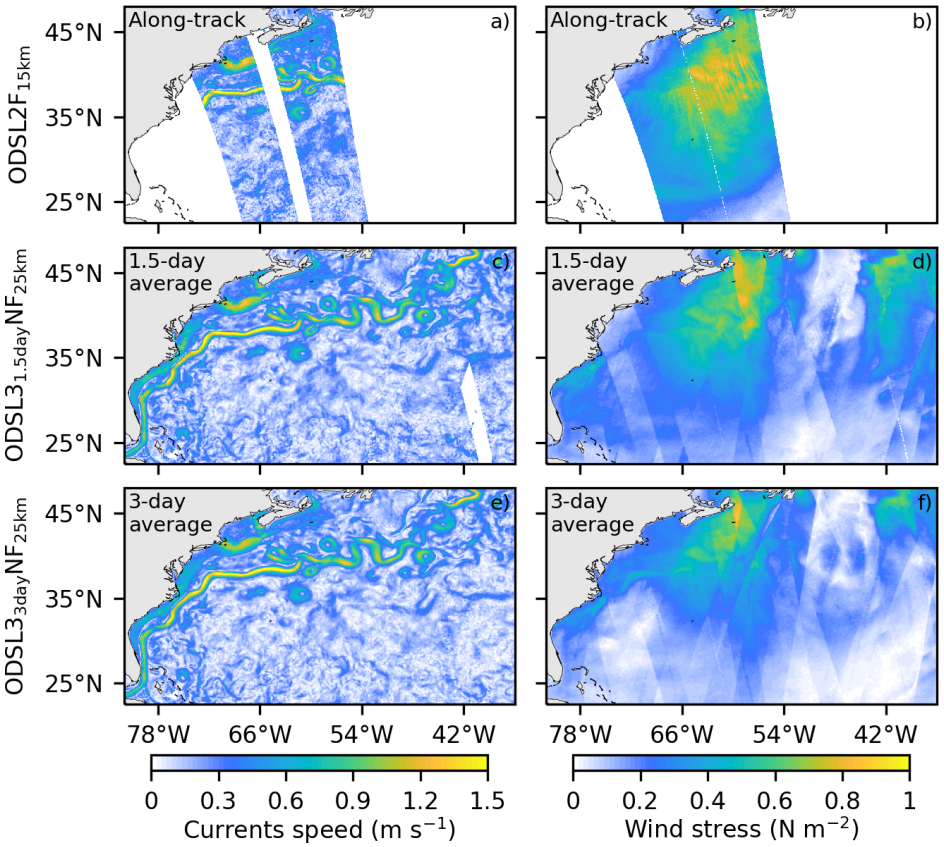

Figure 4. Comparison of the current speed (**first column**) and wind stress (**second column**) from the different datasets obtained through the ODYSEA simulator. Examples for the ODSL2NF$_{15km}$, ODSL3$_{1.5day}$NF$_{25km}$, and ODSL3$_{3day}$NF$_{25km}$ datasets are shown across different rows.

2.4. Satellite "Like" Products

An important part of this work involves comparing the future performance of ODYSEA with contemporaneous satellite missions. Therefore, we also generate datasets that mimic daily altimeter estimations of gridded surface currents from CMEMS [Copernicus Marine Environment Monitoring Service; [21,65]] and wind stress from QuikSCAT [66] by filtering the reference simulation in space and time. The Altimeterlike dataset is generated by applying a 7-day running window and an 85 km diameter spatial filter to the sea level height [13]. Subsequently, surface currents are computed through the application of the geostrophic balance, thus excluding ageostrophic motions as Ekman and cyclogeostrophic currents. The QuikSCATlike dataset is derived by applying a 1-day running mean filter and a 100 km diameter spatial filter to the wind stress components [8,28,67]. We also define the Obslike dataset as a combination of the Altimeterlike and QuikSCATlike datasets. It is important to note that these "like" products are generated by only applying spatial and temporal filters to the reference simulation, without incorporating any random noise. A summary of the filters applied to the reference experiment is shown in Table 2.

Table 2. Time and spatial filters applied to the reference simulation to produce the following "like" datasets: Altimeterlike, QuikSCATlike, and Obslike. Spatial filter values correspond to the filter diameter.

	Surface Currents		Winds and Stress	
Datasets	**Temporal Filter**	**Spatial Filter**	**Temporal Filter**	**Spatial Filter**
Altimeterlike	7 days	85 km	–	–
QuikSCATlike	–	–	1 day	100 km
Obslike	7 days	85 km	1 day	100 km

2.5. Kinetic Energy Fluxes

ODYSEA will be able to concurrently measure surface currents and wind stress. This dual functionality enables us to compute not only horizontal energy fluxes of surface currents but also the flux of kinetic energy between the ocean and the atmosphere, i.e., the wind work. In this study, both energy fluxes are computed using coarse-graining decomposition [68].

The coarse-graining method allows the energy flux related to a certain spatial scale to be estimated [18,38,68–72]. The method is based on the separation between large and small scales around chosen scales L. The signal is separated by applying a two-dimensional running mean with diameter L to a field $\mathcal{F}(x,y)$. This filter results from applying a convolution $\langle \mathcal{F}(x,y) \rangle = \mathcal{C} \times \mathcal{F}(x,y)$ with a top-hat kernel

$$\mathcal{C} = \begin{cases} 1/A, & \text{if } |\mathbf{r}| < L/2, \\ 0, & \text{otherwise.} \end{cases} \tag{1}$$

Here, $A = \pi L^2/4$ is the circular normalization area of diameter L, and $\mathbf{r}$ is the radial position vector [71].

Following [71], applying the convolution to the equation of motion results in a term that allows us to estimate the horizontal energy flux (Π) for a certain scale L:

$$\Pi = -\left(\langle u^2 \rangle - \langle u \rangle^2\right) \frac{\partial \langle u \rangle}{\partial x} + \left(\langle uv \rangle - \langle u \rangle \langle v \rangle\right) \left(\frac{\partial \langle u \rangle}{\partial y} + \frac{\partial \langle v \rangle}{\partial x}\right) + \left(\langle v^2 \rangle - \langle v \rangle^2\right) \frac{\partial \langle v \rangle}{\partial x}, \tag{2}$$

where u and v represent the zonal and meridional components of surface currents, respectively. As mentioned by [68], this term is similar to barotropic instability, which relates to the energy transfer between mean and eddy kinetic energy. With the coarse-grained method, positive values of Π imply an energy flux to smaller scales (forward cascade), whereas negative values imply an energy flux to larger scales (inverse cascade).

Likewise, eddy wind work ($F_e K_e$) is derived from coarse-grained filtered fields:

$$F_e K_e = \left(\langle \tau_x u \rangle - \langle \tau_x \rangle \langle u \rangle\right) + \left(\langle \tau_y v \rangle - \langle \tau_y \rangle \langle v \rangle\right), \tag{3}$$

where τ_x and τ_y correspond to the zonal and meridional components of wind stress relative to surface currents, defined as $\tau = \rho_a C_d U_{rel}^2$. In this expression, ρ_a corresponds to the air density, C_d to the drag coefficient, and $\mathbf{U_{rel}}$ to the wind speed relative to surface currents. Positive values of $F_e K_e$ indicate that the atmosphere is injecting energy into the ocean at the scale L, whereas negative values indicate energy fluxes in the opposing direction [72].

2.6. s_τ Coupling Coefficient

The s_τ coupling coefficient allows us to assess the efficiency of the eddy killing process. Following [5,8], s_τ is computed as the slope of a linear regression between surface ocean

current vorticity anomalies and surface stress curl anomalies. To isolate the mesoscale signal and to remove the atmospheric synoptic variability, anomalies result from a 31-day low-pass filter and a 275 km high-pass filter. It is worth mentioning that regions with quasi-stationary weather conditions, e.g., atmospheric blocking events [73,74], require long averaging times to isolate the mesoscale signal. In order to deal with track overlaps and uncertainties in ODYSEA gridded datasets, s_τ is computed from the noisy level 2 datasets $ODSL3_{1.5day}N$ and $ODSL3_{3day}N$ and then a 25 km low-pass filter is applied.

3. Results

The purpose of this section is to assess the extent to which ODYSEA would capture the surface currents and the associated oceanic kinetic energy, the wind stress, the oceanic cascade of kinetic energy, the exchange of kinetic energy between the (sub)mesoscale eddy and the atmosphere, and the coupling coefficient s_τ. We examine the ability of ODYSEA to capture these fields and aim to understand the impact of uncertainties on their estimation.

3.1. Kinetic Energy of Surface Currents

The surface mean and eddy kinetic energy (MKE and EKE) from the reference simulation, as well as for the ODYSEA and observations-like datasets, are estimated as

$$MKE = 0.5(\overline{u_o}^2 + \overline{v_o}^2), \tag{4}$$

$$EKE = 0.5(\overline{u_o'^2} + \overline{v_o'^2}), \tag{5}$$

where u_o and v_o are the surface currents. The $^-$ represents the annual mean and the $'$ denotes the deviations from the mean. Figure 5 shows the main analysis. The MKE estimated from the reference experiment shows a realistic representation of the Gulf Stream dynamics. The Gulf Stream flows northward along the entire Florida coast up to Cape Hatteras (35°N), where it begins to separate from the coast, veering eastward (Figure 5a). Post-separation, large eddies detach from the Gulf Stream and propagate westward, leading to intense mean mesoscale activity around the Gulf Stream path (up to 0.2 $m^2\ s^{-2}$; Figure 5b).

The Altimeterlike and ODYSEA datasets can reproduce the main spatial patterns of MKE and EKE (Figure 5a–h). However, while the MKE appears to be similar in all the datasets, there are notable discrepancies in the intensity of the EKE estimates. To quantitatively assess these differences over the Gulf Stream, EKE estimates are spatially averaged over the polygon delineated in Figure 5b and visually presented in Figure 5i.

Not surprisingly, and consistent with the literature, the results reveal that Altimeterlike tends to underestimate the EKE by approximately 54%. In contrast, ODSL2, which does not consider the measurement noise, shows a minimal underestimation of the EKE (about 1.5%), showing that the sampling capabilities per se of ODYSEA allow an adequate estimation of the EKE over the Gulf Stream. It is worth noting that, from ODSL2 to ODSL2N, measurement noise spuriously increases the EKE by about 22% (ODSL2N dataset in Figure 5i). In $ODSL2NF_{1.5day}$, however, the spurious EKE is largely removed by applying a 15 km diameter low-pass filter to the surface currents (ODSL2N to $ODSL2NF_{1.5day}$ in Figure 5i).

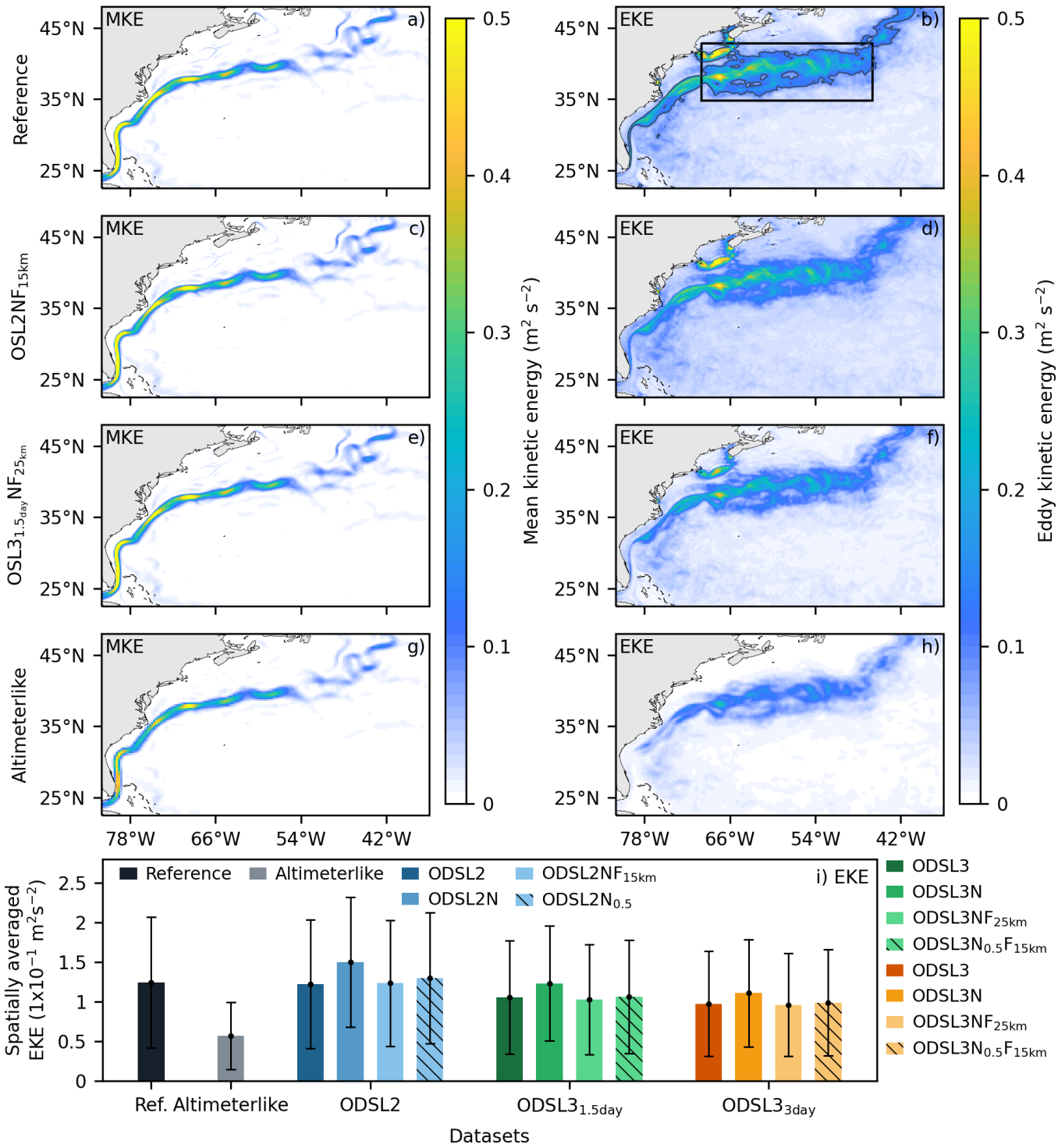

Figure 5. Mean (**first column**) and eddy (**second column**) kinetics over the year 2005 for the reference simulation (**first row**), ODSL2NF$_{15km}$ (**second row**), ODSL3$_{3day}$NF$_{25km}$ (**third row**), and Altimeterlike (**fourth row**) datasets. The mean Gulf Stream system signature, composed of the Gulf Stream and the mesoscale eddies interacting with it, is depicted by the gray contour in panel (**b**), which corresponds to the 0.1 m^2 s^{-2} eddy kinetic energy level. The spatially averaged (bars) eddy kinetic energy over the black polygon in (**b**) is depicted for all datasets at the bottom axes. The standard deviation is indicated by the error bars.

Time averages used for ODSL3 datasets have large consequences in the estimation of EKE. On the one hand, the ODSL3$_{1.5day}$ and ODSL3$_{3day}$ datasets underestimate the EKE by about 15% and 20%, respectively. However, the gridded products of surface currents and wind stress are essential for computing, for example, air–sea coupling coefficients or coarse-

grained energy fluxes. On the other hand, time averages help to reduce uncertainties related to noise in the EKE calculation (Figure 5i). The time-averaged noise datasets, ODSL3$_{1.5day}$N and ODSL3$_{3day}$N, increase EKE estimates from the noise-free datasets by only 16% and 15%, respectively, while EKE estimates from ODSL2 to ODSL2N increase by 22%. Finally, the effect of noise on EKE estimation is mitigated by applying a 25 km low-pass spatial filter to ODSL3$_{1.5day}$N and ODSL3$_{3day}$. Despite the underestimation of the EKE at various degrees depending on the considered dataset, ODYSEA should improve its representation compared to current altimeter estimations.

While spatial filters help to reduce measurement noise, they also have the disadvantage of reducing the fine-scale variability of ocean currents. To better characterize which scales are effectively measured by ODYSEA, a two-dimensional co-spectral analysis is performed on the KE to evaluate the performance of the ODYSEA datasets (Figure 6). The analysis reveals that all ODYSEA datasets accurately capture the KE at the large mesoscale (wavelengths larger than 100 km) and exhibit energy decay rates around k^{-2} (Figure 6). Nevertheless, the sampling capabilities of ODYSEA can lead to a 20% underestimation of energy across wavelengths around 50 km (ODSL3$_{1.5day}$ and ODSL3$_{3day}$ in Figure 6a).

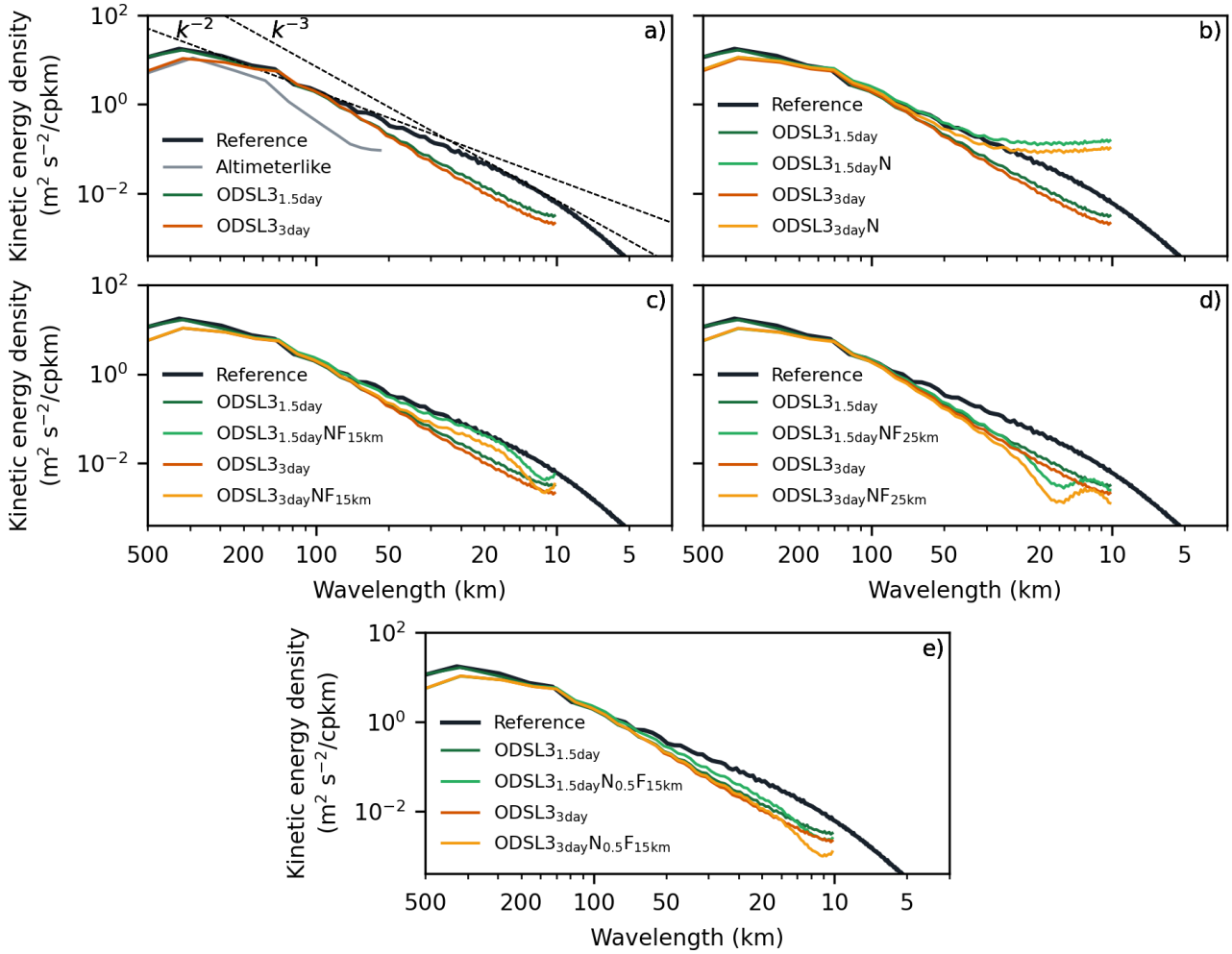

Figure 6. Kinetic energy wave number spectra estimations for the reference simulation, and the Altimeterlike and ODYSEA gridded products over the black polygon depicted in Figure 5a. Consequences related to time averages in ODYSEA are depicted in (**a**), while the consequences related to measurement noise are depicted in (**b**). Consequences related to spatial filters are depicted in (**c**,**d**). The consequences of halving the measurement noise and applying a 15-km spatial filter are depicted in (**e**). Theoretical energy dissipation rates of k^{-2} and k^{-3} are depicted with segmented lines in (**a**).

In $ODSL3_{1.5day}N$ and $ODSL3_{3day}N$, measurement noise leads to a significant overestimation of kinetic energy levels at wavelengths shorter than 80 km (Figure 6b). Consistent with previous analyses, the application of 15 and 25 km low-pass spatial filters (Figure 6c,d) effectively attenuates these spurious kinetic energy levels. While the 15 km spatial filter reduces noise effects, particularly at scales smaller than 50 km wavelength, the energy estimates for $ODSL3_{1.5day}NF_{15km}$ and $ODSL3_{3day}NF_{15km}$ still show an overestimation compared to the noise-free datasets ($ODSL3_{1.5day}$ and $ODSL3_{3day}$) around 20 km wavelength. In contrast, the 25 km spatial filter, though reducing the effective resolution of ODYSEA to about 35 km, yields more accurate energy level estimates at smaller wavelengths, with an underestimationg of only about 7% observed at wavelengths around 50 km. Despite the consequences of spatial and temporal filters being applied to ODYSEA datasets, these filters largely improve the representation of the kinetic energy in comparison with the Altimeter-like dataset, which underestimates energy estimations by about 75–85% at wavelengths between 100 and 50 km and fails to detect smaller-scale features.

3.2. Surface Wind Stress

The wind stress time mean and standard deviation for the reference simulation, as well as for the QuikSCAT-like and ODYSEA datasets, are shown in Figure 7. In the reference simulation, mean wind stress values exceed 0.05 N m^{-2} above 35°N and below 25°N, while weaker values (less than 0.025 N m^{-2}) are observed around 30°N (Figure 7a). Regarding the wind stress variability, it shows a standard deviation greater than 0.2 N m^{-2} above 33°N, with more intense values (greater than 0.3 N m^{-2}) throughout the Gulf Stream (gray contour in Figure 7b).

Mean wind stress conditions are accurately reproduced by QuikSCATlike and ODYSEA datasets (Figure 7a,c,e,g). While these datasets effectively capture the spatial distribution of strong wind stress anomalies (larger than 0.2 N m^{-2}), notable differences emerge when spatially averaging the standard deviation over the polygon depicted in Figure 7a. QuikSCATlike tends to underestimate wind stress variability by approximately 17% over the Gulf Stream region (Figure 7i). In contrast, the sampling capabilities of ODYSEA allow reliable estimations of the wind stress variability across the Gulf Stream, albeit with a slight underestimation of about 5% in ODSL2 with respect to the reference simulation (Figure 7i).

Moreover, because ODYSEA allows wind speed noise levels below 1 m s^{-1}, the standard deviation increases by only 5% when considering the parameterized noise, and is reduced to 3% when applying a 15 km low-pass spatial filter (ODSL2, ODSL2NF, and $ODSL2NF_{15km}$ in Figure 7i).

Conversely, the $ODSL3_{1.5day}$ and $ODSL3_{3day}$ datasets significantly underestimate the wind stress standard deviation compared to ODSL2 (30 and 40%, respectively). This significant underestimation is primarily due to the time averages used to combine along-track data to construct the gridded products, which limits their ability to capture the transient variability in atmospheric dynamics, such as storms, which evolve faster than ocean dynamics [28]. With respect to measurement noise in wind stress, it does not appear to play a critical role in masking atmospheric dynamics.

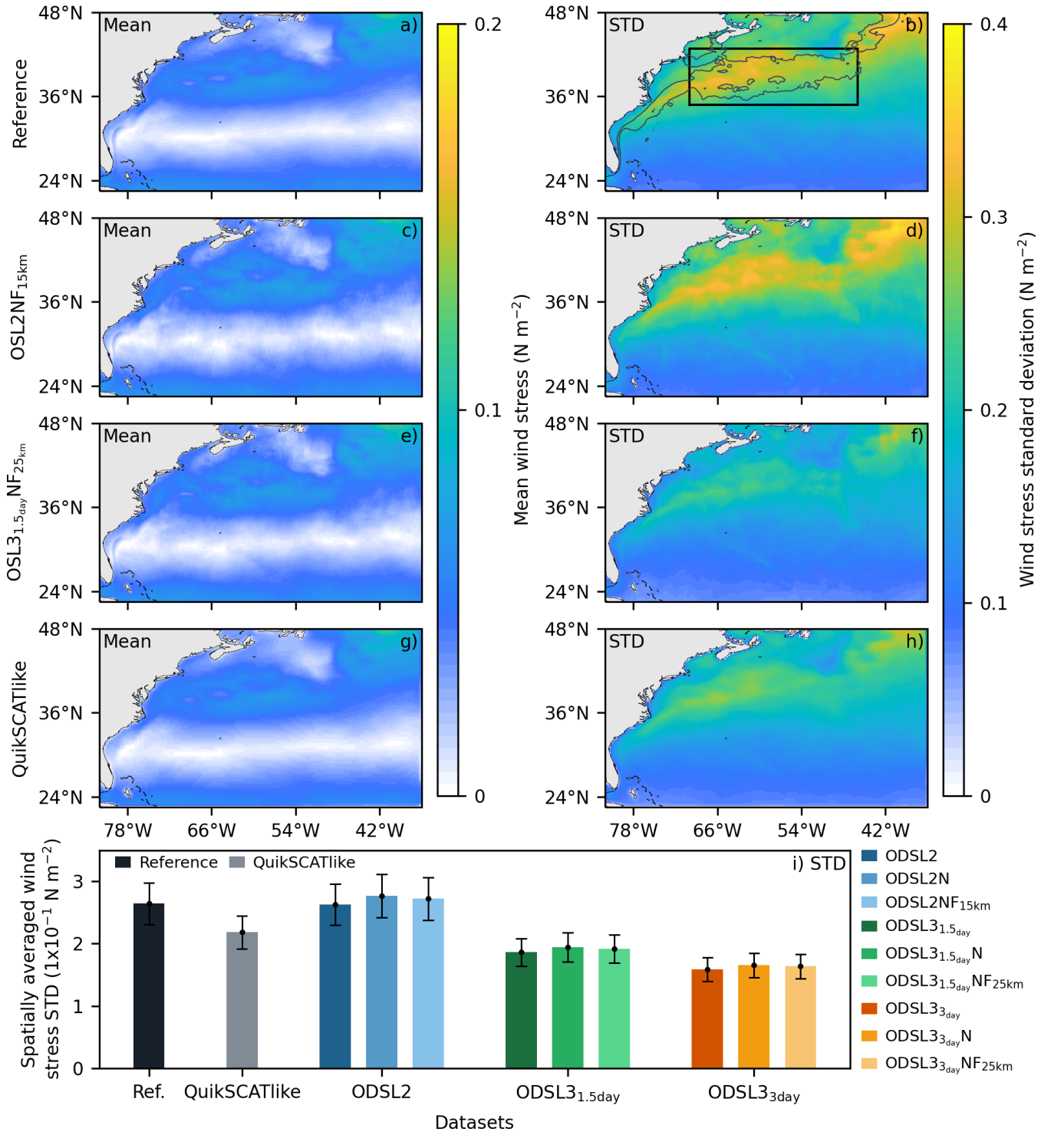

Figure 7. Mean (**first column**) and standard deviation (**second column**) of the wind stress over the year 2005 for the reference simulation (**first row**), ODSL2NF$_{15km}$ (**second row**), ODSL3$_{1.5day}$NF$_{25km}$ (**third row**), and QuikSCATlike (**fourth row**) datasets. The mean Gulf Stream system signature, composed by the Gulf Stream and the mesoscale eddies interacting with it, is depicted by the gray contour in panel (**b**), which corresponds to the 0.1 m^2 s^{-2} eddy kinetic energy level (Figure 5b). The spatially averaged standard deviation (STD) over the black polygon in (**b**) is depicted for all datasets in the bottom panel (**i**).

3.3. Cascade of Kinetic Energy

Following [38], Figure 8 shows the estimates of the surface cascade of kinetic energy for each dataset obtained using a coarse-grained approach [68]. Figure 8a shows the spatially averaged kinetic energy flux over the polygon depicted in Figure 8b, while Figure 8b–i exhibit the spatial distribution of horizontal energy fluxes at small (20 km) and large (150 km) scales.

In agreement with [38], the reference simulation shows predominant forward cascade energy fluxes on scales smaller than 50 km over the Gulf Stream region (Figure 9a), with a peak around 10 km scales. The spatial distribution of horizontal energy fluxes at the small scale (20 km; Figure 9b) shows positive energy fluxes stronger than 100 mW m^{-2} km east of the Gulf Stream separation. Additionally, the figure exhibits a less intense forward cascade of about 50 mW/m^{-2} km west of the Gulf Stream separation. The forward cascade of energy is driven by nonlinear interactions between balanced and unbalanced currents [18], which align with the large-scale meandering patterns of positive energy fluxes all over the Gulf Stream (gray contours in Figure 9a). However, as pointed out by [38], forward cascade energy fluxes are also influenced by the interaction of internal tides and unbalanced motions. On scales larger than 50 km, as expected, there is a strong inverse cascade of energy with a peak at about 160 km. Unlike the forward cascade, the inverse cascade is driven by balanced (mostly geostrophic) currents [13]. The spatial distribution of horizontal energy fluxes on the large scale (150 km; Figure 8c), in spite of being dominated by the inverse cascade, reveals alternating forward and inverse cascade energy fluxes all along the Gulf Stream (gray contour in Figure 8c). It is worth mentioning that these results (Figure 9c) appear noisy compared to those of [38] because the energy cascades are estimated for only 1 year instead of the 5 years in [38].

Regarding the Altimeterlike product, it does not show any significant forward energy cascade (Figure 8a). This can be explained by the inherent limitations of Altimeter. On the one hand, Altimeter is heavily smoothed [26] and, therefore, cannot resolve fine-scale eddies. On the other hand, Altimeter lacks the ageostrophic currents that are essential to capture the forward cascade of energy in the Gulf Stream [18,38]. Consistent with previous studies, e.g., [13,25], the inverse cascade energy fluxes in Altimeterlike are largely underestimated with respect to the reference simulation and shifted to larger scales, with the most intense values around 400 km. A comparison of the spatial distribution of horizontal energy fluxes at the 150 km scale provides valuable insights into understanding these differences (Figure 8c,i). The comparison reveals that the weak inverse cascade energy fluxes in Altimeterlike (Figure 8i) result from weaker and alternating positive-negative energy fluxes (less than 50 mW / m^2 km), which lack the predominant negative energy fluxes seen in the reference simulation (Figure 8b).

For ODYSEA, as explained in Section 2, the energy cascades are estimated using only the L2 product. As shown in Figure 8a, the $ODSL3_{1.5day}$ and $ODSL3_{3day}$ datasets clearly underestimate the forward and inverse cascade energy with respect to the reference simulation. This discrepancy is related to the limitations of ODYSEA in capturing the strong and positive forward cascade energy fluxes at the small scale (Figure 8d,f) and the predominant inverse cascade energy fluxes at the large scale (Figure 8e,g) in comparison to the reference simulation (Figure 8b,c). The main cause of these underestimations is mainly related to the sampling capacities of ODYSEA, because the differences related to noise, as well as temporal and spatial filters, only oscillate by about 17% when compared with the reference simulation (Figure 8a). This shows that the measurement uncertainties in ODYSEA have little effect on the determination of the peak energy fluxes in the region. Therefore, despite the underestimation related to their sampling capabilities, ODYSEA

would largely improve the representation of energy flows and better capture the scales at which the peaks occur compared to Altimeter (Figure 9a).

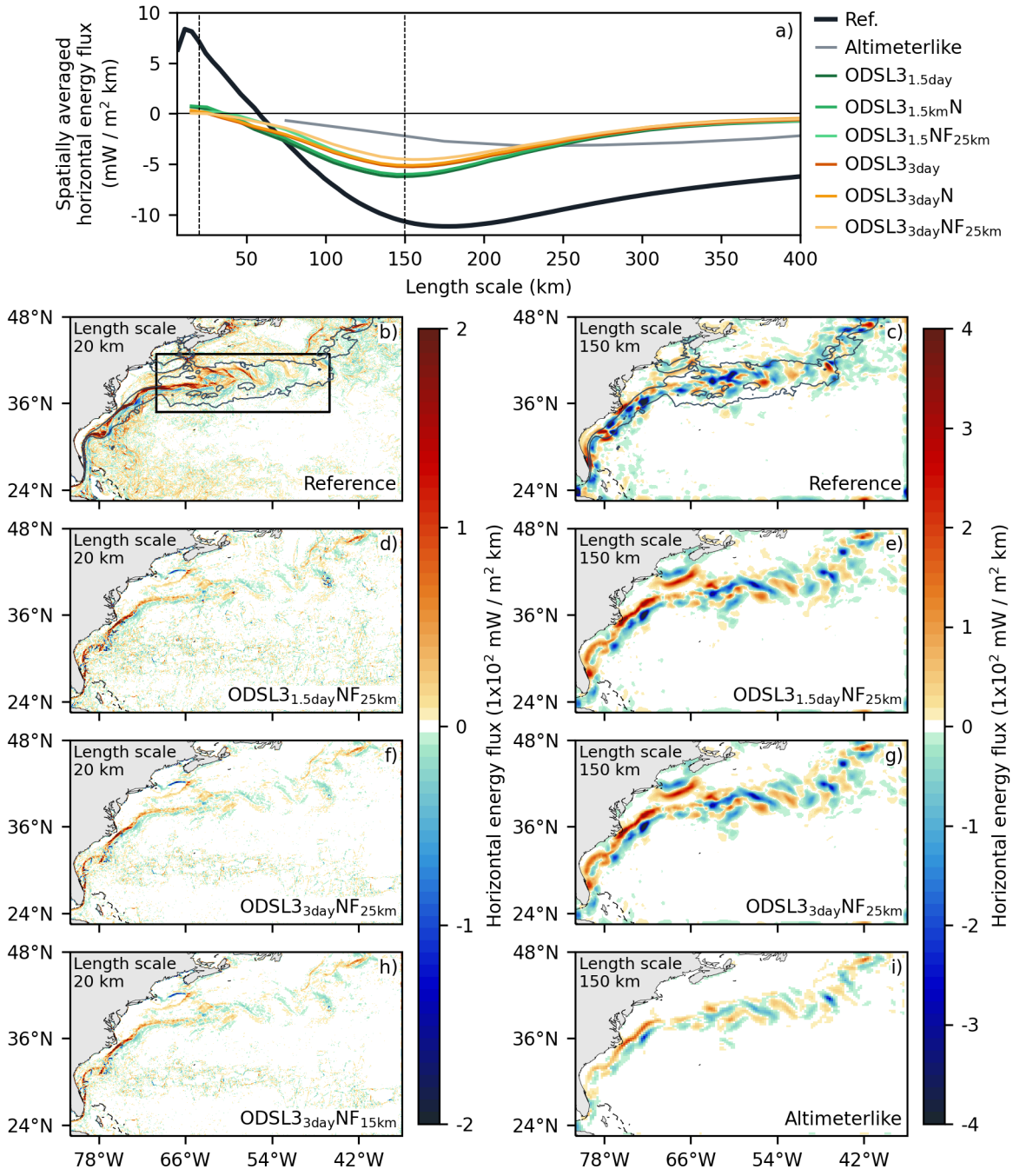

Figure 8. Cascade of kinetic energy. The spatially averaged cascade of kinetic energy over the black polygon in (**b**) is depicted for all datasets at the top axes. Spatial distribution of the cascade of kinetic energy at the 20 m (**first column**) and 150 m (**second column**) scales for the reference simulation (**second row**), ODSL3$_{1.5day}$NF$_{25km}$ (**third row**), and ODSL3$_{3day}$NF$_{25km}$ (**fourth row**). The spatial distribution of the cascade of kinetic energy at the 20 m scale for ODSL3$_{3day}$N$_{0.5}$F$_{25km}$ is shown in (**g**), whereas the cascade of kinetic energy at the 150 m scale for Altimeterlike is shown in (**i**). The mean Gulf Stream system signature, composed of the Gulf Stream and the mesoscale eddies interacting with it, is depicted by the gray contour in panel (**b**), which corresponds to the 0.1 m^2 s^{-2} eddy kinetic energy level (Figure 5b).

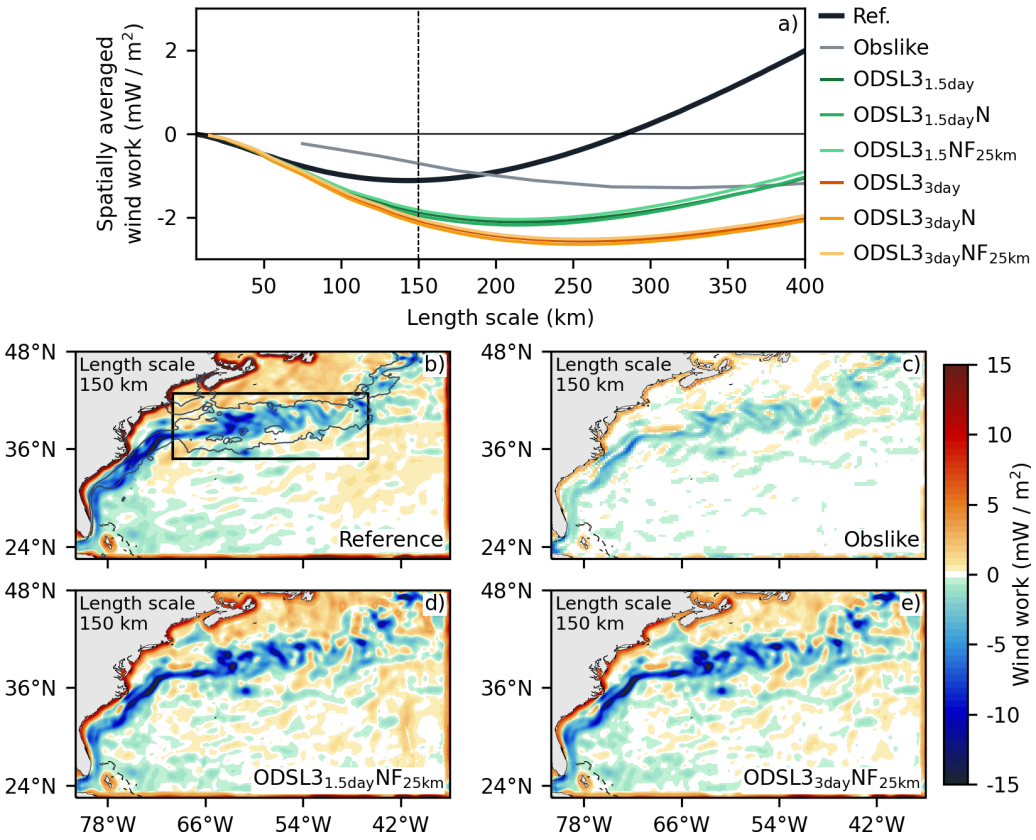

Figure 9. The spatially averaged wind work over the black polygon in (**b**) is depicted for all datasets at the top panel. Spatial distribution of wind work at 20 m scale for reference simulation (**b**), Obslike (**c**), ODSL3$_{1.5day}$NF$_{25km}$ (**d**), and ODSL3$_{3day}$NF$_{25km}$ (**e**). The mean Gulf Stream system signature, composed of the Gulf Stream and the mesoscale eddies interacting with it, is depicted by the gray contour in panel (**b**), which corresponds to the 0.1 m^2 s^{-2} eddy kinetic energy level (Figure 5b).

3.4. Kinetic Energy Flux Between the Ocean and the Atmosphere

Spatially averaged coarse-grained wind work estimations for the reference simulation and Obslike and ODYSEA datasets are depicted in Figure 9a, while their spatial distribution at the 150 km scale is depicted in Figure 9b–e. In the reference simulation, energy fluxes from the ocean to the atmosphere (negative wind work) dominate on scales up to 300 km, with peak intensities (-1.1 mW/m^2) observed at about 150 km (Figure 9a). Negative wind work energy fluxes at these scales are mainly related to the geostrophic eddy wind work, e.g., the sink of energy from the oceanic eddies to the atmosphere [5,7,9,11]. However, because the wind work in the reference simulation is computed as a function of total currents, it includes the contribution of both geostrophic and ageostrophic currents. Ageostrophic eddy wind work fluxes around the 150 km scale are characterized by the interaction of winds and wind-driven currents with similar directions, resulting in positive energy fluxes [5,75], i.e., energy fluxes from the atmosphere to the ocean. This relationship can be observed by comparing the wind work maps in Figure 9b and the EKE maps in Figure 5, which shows that positive wind work in the reference simulation occurs mainly over regions of weak (sub)mesoscale activity.

In contrast, and in agreement with [72], Obslike shows the most negative energy fluxes (1.3 mW/m^2) at scales between 300 and 350 km (Figure 9a). The shift of peak energy fluxes to large scales in altimetric gridded products is mainly due to the ability of altimeter constellations to reproduce mesoscale fluxes. This phenomenon was demonstrated by [25], who found that applying time and space filters to high-resolution numerical simulations to mimic altimetric gridded products results in a shift of energy flux peaks to larger scales. In

particular, the peak wind work estimate from Obslike is about 13% of that from the reference simulation, despite heavily smoothed surface flows. This is because, unlike the reference simulation, Obslike does not take into account ageotrophic currents. Consequently, as shown in Figure 9c, Obslike lacks the positive wind work energy fluxes needed to balance the energy fluxes from (sub)mesoscale eddies into the atmosphere.

Although, to a lesser extent, negative energy flux peaks are shifted to larger scales in the ODYSEA datasets with respect to the original data, occurring at scales around 200 km in $ODL2_{1.5day}$ and 250 in $ODL2_{3day}$ (Figure 9a), a comparison of wind work estimations for the ODYSEA datasets suggests that energy flux peaks are more sensitive to the sampling capacities of ODYSEA and the applied time filters than to measurement noise and the spatial filters used to address it. As a result, the spatially averaged energy fluxes in the $ODL2_{1.5day}$ and $ODL2_{3day}$ datasets are about 1.9 and 2.3 times larger, respectively, than those in the reference simulation. This overestimation results from the reduced sampling capabilities of ODYSEA, and the applied time filters diminish the strength of ageostrophic wind work energy fluxes (Figure 9b,d,e), which counterbalance negative energy fluxes from (sub)mesoscale eddies to the atmosphere. However, despite these limitations, the scale and spatial distribution of the wind work energy flux peak are improved compared to contemporaneous satellite estimates.

3.5. s_τ Coupling Coefficients

A comparison of s_τ coupling coefficients from the reference simulation and the ODYSEA and Obslike datasets is depicted in Figure 10. Consistent with [5,8,23], the reference simulation shows predominantly negative s_τ values over the Gulf Stream region (Figure 10a). Negative s_τ estimations mainly oscillate around -2.8×10^{-4} N s m^{-3}, with the strongest values reaching up to -4×10^{-4} N s m^{-3} over the Gulf Stream (black contour in Figure 10a). By considering positive and negative s_τ values over the region depicted by the black rectangle in Figure 10a, the s_τ spatial average corresponds to -1.8×10^{-4} N s m^{-3}. Interestingly, these coupling coefficient values are stronger than in, e.g., [5,23]. This could be due to differences in the simulation and in the computation of s_τ. First, the simulation used in this study spans only 1 year (vs. 5 years in [23]) and we consider both geostrophic and ageostrophic currents, including some submesoscale currents in the computation of s_τ. As demonstrated by [76] for the Caribbean Sea, the eddy killing efficiency (estimated through the s_τ coupling coefficient) can be 32% larger at the submesoscale than at the mesoscale. Secondly, surface gravity waves, through a change of roughness, may also impact the efficiency of CFB, which could be reflected in a stronger s_τ.

In contrast, and in agreement with [13,23], negative s_τ estimations from Obslike are mostly around 1.2×10^{-4} N s m^{-3}, reaching values of up to 2×10^{-4} N s m^{-3} over the Gulf Stream region (Figure 10b). On average, s_τ values in Obslike are about 20% lower than in the reference simulation over the Gulf Stream region (Figure 10i). This underestimation results from the space and time filters applied to mimic Altimeter and QuikSCAT observations, but also because s_τ estimations from altimeter gridded products lack the contribution of ageostrophic motions.

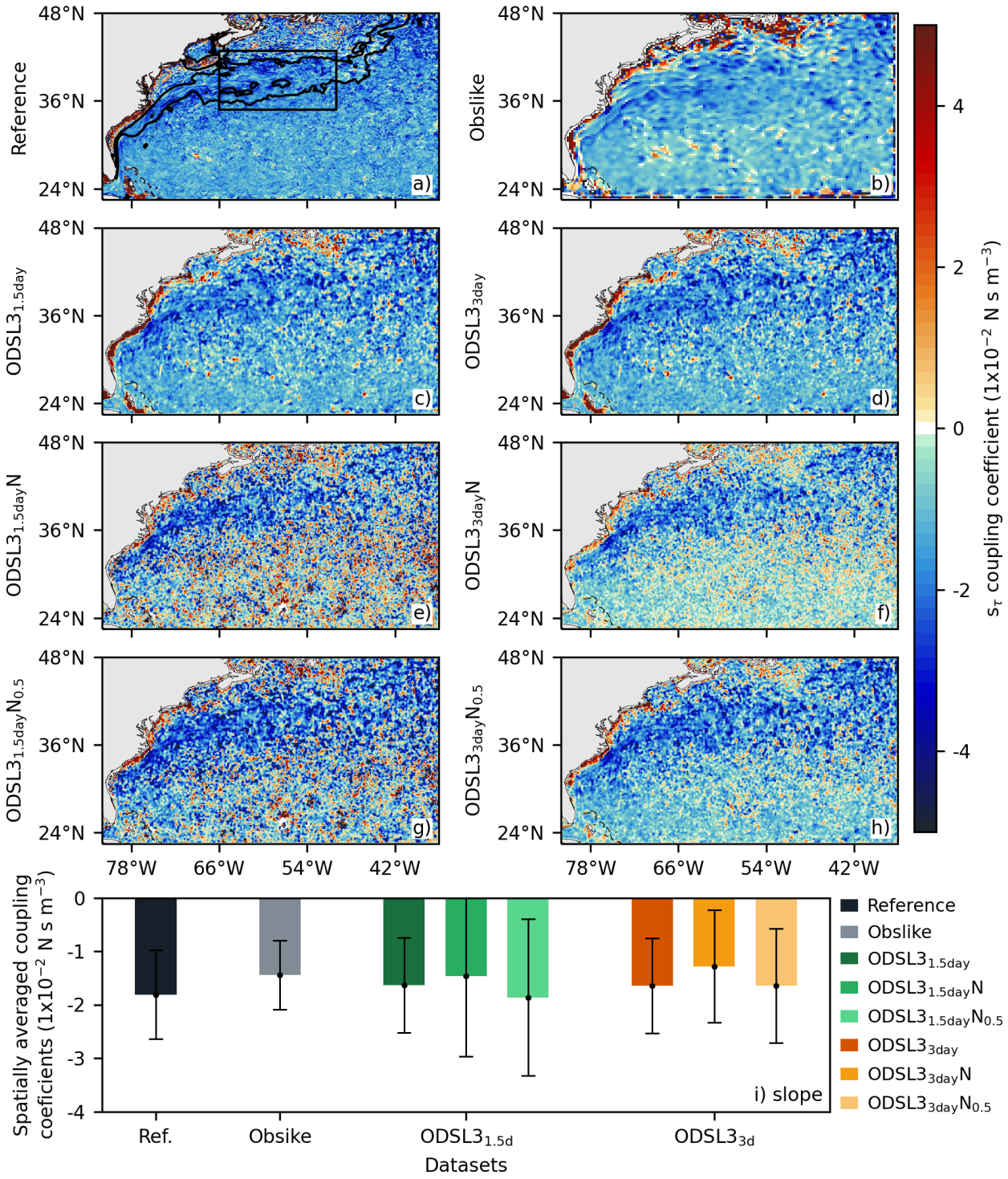

Figure 10. s_τ coupling coefficients for the reference simulation (**a**) and the Obslike (**b**) and ODYSEA datasets (**c–h**). The mean Gulf Stream system signature, composed of the Gulf Stream and the mesoscale eddies interacting with it, is depicted by the black contour in panel (**b**), which corresponds to the 0.1 m^2 s^{-2} eddy kinetic energy level (Figure 5b). The black squared polygon delimits the Loop Current region. Spatially averaged values over the polygon depicted in (**a**) are shown in the bottom panel.

The ODYSEA datasets ODSL3$_{1.5_{day}}$ and ODSL3$_{3_{day}}$, which do not include noise and spatial filters, show predominantly negative coupling coefficients of about 2×10^{-4} N s m^{-3} (Figure 10c,d), reaching up to 4×10^{-4} N s m^{-3} over the Gulf Stream (black contour in Figure 10a). Compared to the reference simulation, ODSL31.5$_{day}$ and ODSL33$_{day}$ show

s_τ values over the Gulf Stream region that are only 10% and 9.5% lower, respectively (Figure 10i). The small difference between $ODSL3_{1.5_{day}}$ and $ODSL3_{3_{day}}$ suggests that the s_τ estimates are more sensitive to ODYSEA's sampling capabilities than to the temporal averages used to construct the gridded datasets. In contrast, measurement noise has a larger effect on the s_τ estimates. On the one hand, this results in strong and alternating positive–negative noisy s_τ values outside the Gulf Stream in $ODSL3_{1.5_{day}}N$ (Figure 10e), increasing the standard deviation by 69% compared to $ODSL3_{1.5_{day}}$. However, these noisy s_τ values seem to cancel each other out, as there is only a 10% underestimation of s_τ from $ODSL3_{1.5_{day}}$ to $ODSL3_{1.5_{day}}N$ over the Gulf Stream region (Figure 10i). On the other hand, the amplitude of the noisy s_τ values seems to be reduced by the 3-day temporal filter in $ODSL3_{3_{day}}N$ (Figure 10e,f). As a consequence, the standard deviation of s_τ over the Gulf Stream region is only 18% larger from $ODSL3_{3_{day}}$ to $ODSL3_{3_{day}}N$ (Figure 10i), and also results in a 22% underestimation of the s_τ mean (Figure 10i).

The results above demonstrate that sampling capabilities and measurement noise prevent ODYSEA from improving s_τ coupling coefficient estimation from contemporaneous satellite missions. Sampling limitations restrain ODYSEA from accurately reconstructing atmospheric features such as storms in L2 datasets, while measurement uncertainties related to ocean currents result in strong noisy s_τ estimations. Nevertheless, the following section will explore how halving the noise in surface ocean current estimations could enhance the accuracy of ocean kinetic energy and s_τ coupling coefficient estimations.

3.6. Consequences of Halving Measurement Noise

As shown in Sections 3, 3.1 and 3.5, the eddy kinetic energy and coupling coefficient estimates from the ODYSEA L2 datasets are strongly affected by the measurement noise. Spatial filters may assist in addressing this issue, although such filters also reduce the effective resolution of the ODYSEA measurements (Figure 6). Nevertheless, halving the measurement noise could improve the performance of ODYSEA and, consequently, the eddy kinetic energy and coupling coefficient estimates. As shown in Figure 5i, $ODSL2N_{0.5}$ overestimates ODSL2 by only about 6%, a significant improvement over the 22% overestimation of ODSL2N. It is worth noting that applying a 15 km spatial filter to ODSL2N ($ODSL2NF_{15_{km}}$) results in closer estimates of the spatially averaged eddy kinetic energy over the Gulf Stream region of ODSL2, but at the cost of reducing its effective resolution via the spatial filter.

For the ODYSEA L2 datasets, applying a 15 km spatial filter to noisy 1.5- and 3-day temporally filtered gridded products ($ODSL3_{1.5_{day}}N_{0.5}F_{15km}$ and $ODSL3_{3_{day}}N_{0.5}F_{15km}$) does not affect the eddy kinetic energy statistics over the Gulf Stream region (Figure 5i). In addition, the application of the 15 km spatial filter enhances the effective resolution of the products when compared to their counterparts with full noise and 25 km spatial averaging ($ODSL3_{1.5_{day}}NF_{25km}$ and $ODSL3_{3_{day}}NF_{25km}$; Figure 6d,e). However, a co-spectral analysis shows that 1.5-day averages cannot fully suppress measurement uncertainties on scales between 20 and 50 km. At these scales, the kinetic energy density in $ODSL3_{1.5_{day}}N_{0.5}F_{15km}$ is about 30% larger than in $ODSL3_{1.5_{day}}$ (Figure 6e). These results indicate that halving the measurement uncertainties in surface currents can be effectively handled by a combination of 3-day temporal and 15 km spatial filters (Figures 5i and 6e).

The reduction in the measurement noise also improves the representation of the s_τ coupling coefficients in the ODSL3 datasets. The occurrence of noisy s_τ coupling coefficients outside the Gulf Stream is largely reduced from $ODSL3_{1.5_{day}}N$ to $ODSL3_{1.5_{day}}N_{0.5}$ (Figure 10e,g). Nevertheless, the averaged s_τ coupling coefficient over the Gulf Stream region is about 12% stronger in $ODSL3_{1.5_{day}}N_{0.5}$ than in $ODSL3_{1.5_{day}}$, indicating that halved measurement noise introduces a bias in s_τ when estimated from 1.5-day temporally aver-

aged ODYSEA datasets. Instead, noisy s_τ coupling coefficients outside the Gulf Stream are strongly reduced from $\mathrm{ODSL3}_{1.5_{\mathrm{day}}}\mathrm{N}$ to $\mathrm{ODSL3}_{3_{\mathrm{day}}}\mathrm{N}$. Therefore, the calculation of s_τ coupling coefficients from 3-day averaged datasets with halved measurement noise ($\mathrm{ODSL3}_{3_{\mathrm{day}}}\mathrm{N}_{0.5}$) leads to less noisy s_τ values outside the Gulf Stream and thus to more similar statistics over the Gulf Stream region compared to the $\mathrm{ODSL3}_{3_{\mathrm{day}}}$ dataset.

Finally, although the measurement noise depends largely on the length of the ODYSEA antenna [29], the antenna length must meet the NASA Earth Explorer-class mission specifications [28]. Therefore, a balance must be found between reducing the noise in the measurements by increasing the antenna length and ensuring compliance with NASA requirements.

4. Discussion and Conclusions

In this study, we analyzed the capabilities of the future ODYSEA satellite mission to estimate surface currents and wind stress, the cascade of surface kinetic energy, kinetic energy fluxes between the ocean and the atmosphere, and the efficiency of the eddy killing mechanism through the s_τ coupling coefficient. To this end, we generated synthetic data from a high-spatial-resolution coupled ocean–atmosphere–wave simulation with the ODYSIM simulator. Several datasets were developed from the ODYSIM along-track results. These included gridded datasets generated by merging along-track data using 1.5- and 3-day time averages, and the inclusion of parametric measurement noise and spatial filters to address it. These datasets were compared to the reference simulation to evaluate the measurement capabilities of ODYSEA, as well as observation-like datasets that mimic altimeter and scatterometer observations to evaluate the performance of ODYSEA relative to contemporaneous satellite measurements.

The ODYSEA datasets effectively reproduce the spatial distribution and intensity of the mean kinetic energy over the Gulf Stream. However, there are notable differences in the EKE estimates in some of the ODYSEA datasets. While its sampling capabilities allow ODYSEA to adequately estimate the EKE from along-track data, measurement noise leads to significant discrepancies. The noise spuriously increases EKE estimates by 22% over the Gulf Stream region. This can be mitigated by applying 15 km spatial filters, but at the cost of reducing the effective resolution of the measurements. As expected, gridded datasets from 1.5- and 3-day temporal averages diminish EKE estimations by 15 and 20%, respectively. This underestimation mainly occurs over scales of around 50 km, where the KE is underestimated by about 20%. Not surprisingly, measurement noise in gridded products is more evident at scales smaller than 50 km. However, measurement noise can be handled by 25 km spatial filters without significant impact on EKE estimates over the Gulf Stream. However, this means that ODYSEA will not be able to capture submesoscale currents. Despite the limitations, ODYSEA will be able to improve the representation of mesoscale features compared to contemporaneous altimetric gridded products, which are unable to capture features smaller than 100 km in diameter [24–27].

Forward and inverse energy cascade peaks are largely underestimated in ODYSEA gridded products. The underestimation of the forward energy cascade, which occurs at scales around 20 km, coincides with a similar underestimation of the KE energy density at these scales. Measurement noise and temporal and spatial filters do not significantly modulate ODYSEA estimates of the spatially averaged cascade of KE over the Gulf Stream region. However, they do shift the inverse cascade peaks to larger scales. These results highlight the critical importance of the measurement capabilities of ODYSEA, particularly in terms of spatial resolution and sub-sampling accuracy, as these factors contribute to the underestimation of forward and inverse energy cascade peaks. However, despite the underestimation of forward and inverse energy cascade peaks, ODYSEA notably improves on contemporaneous satellite measurements that largely underestimate the EKE

and cascade of KE over the Gulf Stream region. In addition, ODYSEA's 4-day repeat cycle and 1700 km measurement swath would enhance the sampling capabilities of the recently launched Surface Water and Ocean Topography (SWOT) satellite mission. SWOT is a nadir altimeter capable of inferring surface geostrophic currents through the geostrophic balance, with an effective resolution of 15 km. However, its 21-day repeat cycle and two 5 km wide swaths limit its sampling capabilities, allowing it to measure 90% of the globe at least once every 21 days [77]. These constraints prevent SWOT from effectively tracking rapidly evolving mesoscale structures and inhibit it from measuring ageostrophic motions.

In terms of wind stress statistics, ODYSEA along-track datasets can properly reproduce the spatial distribution of mean and standard deviation estimates from the reference simulation. However, gridded products, which are essential for the calculation of coarse-grained wind work and s_τ coupling coefficients, largely underestimate the variability of wind stress. Temporal averaging over 1.5 and 3 days leads to underestimations of 30 and 40%, respectively, compared to the reference simulation. The underestimation of wind stress variability in gridded products is mainly related to the reduced temporal sampling of ODYSEA, which does not allow it to capture the propagation of atmospheric storms. Nevertheless, efforts should be made to construct daily wind stress maps from ODYSEA measurements by following approaches like those of [22,66], who successfully built daily wind stress maps from the synergy between scatterometer observations and numerical reanalysis data.

As reported by [28], ODYSEA effectively reproduces seasonal wind work estimates from along-track measurements. However, the sensitivity of wind work to different spatial scales has not been previously documented. Gridded products from ODYSEA, which result from merging along-track measurements over 1.5- and 3-day periods, tend to underestimate positive wind work energy fluxes, which represent the transfer of energy from the atmosphere to the ocean. This underestimation is mainly due to the filtering of wind-driven currents resulting from the merging of along-track measurements; the longer the time periods used to construct the gridded dataset, the greater the underestimation of positive wind energy fluxes. As the SWOT data may help estimation of the geostrophic currents, future analysis should quantify the effects of ODYSEA's measurement capabilities on the representation of wind work associated with balanced and unbalanced motions, allowing a deeper assessment of ODYSEA's performance in estimating wind work over (sub)mesoscale eddies and wind-driven motions.

Although ODYSEA should improve the representation of s_τ coupling coefficients compared to contemporaneous satellite estimates, given that surface currents and stress have the same effective resolution and are measured simultaneously and at the same location, measurement capabilities and uncertainties prevent ODYSEA from improving the estimation of coupling coefficients compared to current satellite missions. Nevertheless, our study shows that halving the measurement uncertainties will allow ODYSEA not only to improve the representation of surface currents but also, to a greater extent, to improve the accuracy of the s_τ coupling coefficients. Blending the ODYSEA data with other scatterometters and with a reanalysis (as in, e.g., [22]) may also help to improve their representation. In addition, alternatives related to neural networks could be explored to reduce the noise in sea surface current estimates [78].

Finally, additional noise sources, such as rainfall, sea surface temperature, and sea state, should be accounted for in future studies to fully evaluate the performance of Ka-band scatterometers such as ODYSEA [30–34].

Author Contributions: Conceptualization, M.L., L.R., A.W., B.K.A., M.A.B. and E.R.; methodology, M.L. and L.R.; software, M.L. and M.C.; numerical simulation, L.R. and M.C.; A.W. led the development of the ODYSEA simulator; formal analysis, M.L. and L.R.; original draft preparation, M.L. and L.R.; writing—review and editing, all authors contributed equally to this part. All authors have read and agreed to the published version of the manuscript.

Funding: The authors appreciate the support from the CNES (projects THETHYS, M-ODYSEA, and I-CASCADE), the CNRS (LEFE VENUS), the ANR JPI-CLIMATE EUREC4A-OA, and NASA (grants 80GSFC24CA067 and 80NSSC20K1135).

Data Availability Statement: The ODYSEA simulator can be download from https://github.com/awineteer/odysea-science-simulator/ (accessed on 20 June 2023). The coupled model output fields are too large to be retained or publicly archived with available resources. However, the documentation and methods used to support this study are available from Lionel Renault (lionel.renault@ird.fr) at the Laboratoire d'Etudes en Géophysique et Océanographie Spatiales, Toulouse, France.

Acknowledgments: Supercomputing facilities were provided by GENCI projects GEN7298 and GEN13051.

Conflicts of Interest: The authors declare no conflicts of interest.

References

1. Bye, J.A. Chapter 6 Large-Scale Momentum Exchange in the Coupled Atmosphere-Ocean. In *Elsevier Oceanography Series*; Elsevier: Amsterdam, The Netherlands, 1985; pp. 51–61. [CrossRef]
2. Dewar, W.K.; Flierl, G.R. Some Effects of the Wind on Rings. *J. Phys. Oceanogr.* **1987**, *17*, 1653–1667. [CrossRef]
3. Duhaut, T.H.A.; Straub, D.N. Wind Stress Dependence on Ocean Surface Velocity: Implications for Mechanical Energy Input to Ocean Circulation. *J. Phys. Oceanogr.* **2006**, *36*, 202–211. [CrossRef]
4. Seo, H.; Miller, A.J.; Norris, J.R. Eddy–wind interaction in the California Current System: Dynamics and impacts. *J. Phys. Oceanogr.* **2016**, *46*, 439–459. [CrossRef]
5. Renault, L.; Molemaker, M.J.; McWilliams, J.C.; Shchepetkin, A.F.; Lemarié, F.; Chelton, D.; Illig, S.; Hall, A. Modulation of wind work by oceanic current interaction with the atmosphere. *J. Phys. Oceanogr.* **2016**, *46*, 1685–1704. [CrossRef]
6. Luo, J.J.; Masson, S.; Roeckner, E.; Madec, G.; Yamagata, T. Reducing Climatology Bias in an Ocean–Atmosphere CGCM with Improved Coupling Physics. *J. Clim.* **2005**, *18*, 2344–2360. [CrossRef]
7. Renault, L.; Molemaker, M.J.; Gula, J.; Masson, S.; McWilliams, J.C. Control and stabilization of the Gulf Stream by oceanic current interaction with the atmosphere. *J. Phys. Oceanogr.* **2016**, *46*, 3439–3453. [CrossRef]
8. Renault, L.; McWilliams, J.C.; Masson, S. Satellite Observations of Imprint of Oceanic Current on Wind Stress by Air-Sea Coupling. *Sci. Rep.* **2017**, *7*, 17747. [CrossRef]
9. Oerder, V.; Colas, F.; Echevin, V.; Masson, S.; Lemarié, F. Impacts of the Mesoscale Ocean-Atmosphere Coupling on the Peru-Chile Ocean Dynamics: The Current-Induced Wind Stress Modulation. *J. Geophys. Res. Ocean.* **2018**, *123*, 812–833. [CrossRef]
10. Jullien, S.; Masson, S.; Oerder, V.; Samson, G.; Colas, F.; Renault, L. Impact of Ocean–Atmosphere Current Feedback on Ocean Mesoscale Activity: Regional Variations and Sensitivity to Model Resolution. *J. Clim.* **2020**, *33*, 2585–2602. [CrossRef]
11. Renault, L.; McWilliams, J.C.; Penven, P. Modulation of the Agulhas Current retroflection and leakage by oceanic current interaction with the atmosphere in coupled simulations. *J. Phys. Oceanogr.* **2017**, *47*, 2077–2100. [CrossRef]
12. Seo, H.; Kwon, Y.O.; Joyce, T.M.; Ummenhofer, C.C. On the Predominant Nonlinear Response of the Extratropical Atmosphere to Meridional Shifts of the Gulf Stream. *J. Clim.* **2017**, *30*, 9679–9702. [CrossRef]
13. Renault, L.; Marchesiello, P.; Masson, S.; Mcwilliams, J.C. Remarkable control of western boundary currents by eddy killing, a mechanical air-sea coupling process. *Geophys. Res. Lett.* **2019**, *46*, 2743–2751. [CrossRef]
14. Renault, L.; Arsouze, T.; Ballabrera-Poy, J. On the Influence of the Current Feedback to the Atmosphere on the Western Mediterranean Sea Dynamics. *J. Geophys. Res. Ocean.* **2021**, *126*, e2020JC016664. [CrossRef]
15. Larrañaga, M.; Renault, L.; Jouanno, J. Partial Control of the Gulf of Mexico Dynamics by the Current Feedback to the Atmosphere. *J. Phys. Oceanogr.* **2022**, *52*, 2515–2530. [CrossRef]
16. Zhai, X.; Greatbatch, R.J. Wind work in a model of the northwest Atlantic Ocean. *Geophys. Res. Lett.* **2007**, *34*. [CrossRef]
17. Alford, M.H. Revisiting Near-Inertial Wind Work: Slab Models, Relative Stress, and Mixed Layer Deepening. *J. Phys. Oceanogr.* **2020**, *50*, 3141–3156. [CrossRef]
18. Contreras, M.; Renault, L.; Marchesiello, P. Understanding Energy Pathways in the Gulf Stream. *J. Phys. Oceanogr.* **2023**, *53*, 719–736. [CrossRef]

19. Torres, H.S.; Klein, P.; Wang, J.; Wineteer, A.; Qiu, B.; Thompson, A.F.; Renault, L.; Rodriguez, E.; Menemenlis, D.; Molod, A.; et al. Wind work at the air-sea interface: A modeling study in anticipation of future space missions. *Geosci. Model Dev.* **2022**, *15*, 8041–8058. [CrossRef]
20. Delpech, A.; Barkan, R.; Renault, L.; McWilliams, J.; Siyanbola, O.Q.; Buijsman, M.C.; Arbic, B.K. Wind-current feedback is an energy sink for oceanic internal waves. *Sci. Rep.* **2023**, *13*, 5915. [CrossRef]
21. Taburet, G.; Sanchez-Roman, A.; Ballarotta, M.; Pujol, M.I.; Legeais, J.F.; Fournier, F.; Faugere, Y.; Dibarboure, G. DUACS DT2018: 25 years of reprocessed sea level altimetry products. *Ocean. Sci.* **2019**, *15*, 1207–1224. [CrossRef]
22. Bentamy, A.; Fillon, D.C. Gridded surface wind fields from Metop/ASCAT measurements. *Int. J. Remote Sens.* **2011**, *33*, 1729–1754. [CrossRef]
23. Renault, L.; Masson, S.; Oerder, V.; Jullien, S.; Colas, F. Disentangling the Mesoscale Ocean-Atmosphere Interactions. *J. Geophys. Res. Ocean.* **2019**, *124*, 2164–2178. [CrossRef]
24. Chelton, D.B.; Schlax, M.G.; Samelson, R.M. Global observations of nonlinear mesoscale eddies. *Prog. Oceanogr.* **2011**, *91*, 167–216. [CrossRef]
25. Arbic, B.K.; Polzin, K.L.; Scott, R.B.; Richman, J.G.; Shriver, J.F. On Eddy Viscosity, Energy Cascades, and the Horizontal Resolution of Gridded Satellite Altimeter Products*. *J. Phys. Oceanogr.* **2013**, *43*, 283–300. [CrossRef]
26. Amores, A.; Jordà, G.; Arsouze, T.; Le Sommer, J. Up to what extent can we characterize ocean eddies using present-day gridded altimetric products? *J. Geophys. Res. Ocean.* **2018**, *123*, 7220–7236. [CrossRef]
27. Archer, M.R.; Li, Z.; Fu, L.L. Increasing the Space–Time Resolution of Mapped Sea Surface Height From Altimetry. *J. Geophys. Res. Ocean.* **2020**, *125*, 015878. [CrossRef]
28. Torres, H.; Wineteer, A.; Klein, P.; Lee, T.; Wang, J.; Rodriguez, E.; Menemenlis, D.; Zhang, H. Anticipated Capabilities of the ODYSEA Wind and Current Mission Concept to Estimate Wind Work at the Air–Sea Interface. *Remote Sens.* **2023**, *15*, 3337. [CrossRef]
29. Rodriguez, E. On the Optimal Design of Doppler Scatterometers. *Remote Sens.* **2018**, *10*, 1765. [CrossRef]
30. Wineteer, A.; Torres, H.S.; Rodriguez, E. On the Surface Current Measurement Capabilities of Spaceborne Doppler Scatterometry. *Geophys. Res. Lett.* **2020**, *47*, 090116. [CrossRef]
31. Rodríguez, E.; Bourassa, M.; Chelton, D.; Farrar, J.T.; Long, D.; Perkovic-Martin, D.; Samelson, R. The Winds and Currents Mission Concept. *Front. Mar. Sci.* **2019**, *6*, 00438. [CrossRef]
32. Grodsky, S.A.; Kudryavtsev, V.N.; Bentamy, A.; Carton, J.A.; Chapron, B. Does direct impact of SST on short wind waves matter for scatterometry? *Geophys. Res. Lett.* **2012**, *39*, 52091. [CrossRef]
33. Wang, Z.; Stoffelen, A.; Fois, F.; Verhoef, A.; Zhao, C.; Lin, M.; Chen, G. SST Dependence of Ku- and C-Band Backscatter Measurements. *IEEE J. Sel. Top. Appl. Earth Obs. Remote Sens.* **2017**, *10*, 2135–2146. [CrossRef]
34. Stow, J.P.; Bourassa, M.A.; Holbach, H.M. Analyzing Gaps in Hurricane Rain Coverage to Inform Future Satellite Proposals. *Remote Sens.* **2020**, *12*, 2673. [CrossRef]
35. Shchepetkin, A.F.; McWilliams, J.C. The regional oceanic modeling system (ROMS): A split-explicit, free-surface, topography-following-coordinate oceanic model. *Ocean. Model.* **2005**, *9*, 347–404. [CrossRef]
36. Debreu, L.; Marchesiello, P.; Penven, P.; Cambon, G. Two-way nesting in split-explicit ocean models: Algorithms, implementation and validation. *Ocean. Model.* **2012**, *49–50*, 1–21. [CrossRef]
37. Skamarock, W.C.; Klemp, J.B.; Dudhia, J.; Gill, D.O.; Liu, Z.; Berner, J.; Wang, W.; Powers, J.G.; Duda, M.G.; Barker, D.M.; et al. *A Description of the Advanced Research WRF Model Version 4*; National Center for Atmospheric Research: Boulder, CO, USA 2019; p. 145.
38. Contreras, M.; Renault, L.; Marchesiello, P. Tidal modulation of energy dissipation routes in the Gulf Stream. *Geophys. Res. Lett.* **2023**, *50*, e2023GL104946. [CrossRef]
39. Contreras, M. Study of the Kinetic Energy Cycle and Dissipation Pathways in the Gulf Stream. Ph.D. Thesis, Université Paul Sabatier, Toulouse, France, 2023.
40. Soufflet, Y.; Marchesiello, P.; Lemarié, F.; Jouanno, J.; Capet, X.; Debreu, L.; Benshila, R. On effective resolution in ocean models. *Ocean. Model.* **2016**, *98*, 36–50. [CrossRef]
41. Ménesguen, C.; Le Gentil, S.; Marchesiello, P.; Ducousso, N. Destabilization of an Oceanic Meddy-Like Vortex: Energy Transfers and Significance of Numerical Settings. *J. Phys. Oceanogr.* **2018**, *48*, 1151–1168. [CrossRef]
42. Marchesiello, P.; Debreu, L.; Couvelard, X. Spurious diapycnal mixing in terrain-following coordinate models: The problem and a solution. *Ocean. Model.* **2009**, *26*, 156–169. [CrossRef]
43. Lemarié, F.; Kurian, J.; Shchepetkin, A.F.; Jeroen Molemaker, M.; Colas, F.; McWilliams, J.C. Are there inescapable issues prohibiting the use of terrain-following coordinates in climate models? *Ocean. Model.* **2012**, *42*, 57–79. [CrossRef]
44. Large, W.G.; McWilliams, J.C.; Doney, S.C. Oceanic vertical mixing: A review and a model with a nonlocal boundary layer parameterization. *Rev. Geophys.* **1994**, *32*, 363–403. [CrossRef]

45. Lellouche, J.M.; Le GallouDecember, O.; Greiner, E.; Garric, G.; Regnier, C.; Drevillon, M.; Le Traon, P. The Copernicus Marine Environment Monitoring Service global ocean 1/12 physical reanalysis GLORYS12V1: Description and quality assessment. In Proceedings of the Egu General Assembly Conference Abstracts, Vienna, Austria, 8–13 April 2018; Volume 20, p. 19806.
46. Egbert, G.D.; Erofeeva, S.Y. Efficient Inverse Modeling of Barotropic Ocean Tides. *J. Atmos. Ocean. Technol.* **2002**, *19*, 183–204. [CrossRef]
47. Hersbach, H.; Bell, B.; Berrisford, P.; Biavati, G.; Horányi, A.; Muñoz Sabater, J.; Nicolas, J.; Peubey, C.; Radu, R.; Rozum, I.; et al. *ERA5 Hourly Data on Single Levels from 1940 to Present*; Copernicus Climate Change Service: Reading, UK, 2023. [CrossRef]
48. Han, J.Y.; Hong, S.Y.; Kwon, Y.C. The Performance of a Revised Simplified Arakawa–Schubert (SAS) Convection Scheme in the Medium-Range Forecasts of the Korean Integrated Model (KIM). *Weather. Forecast.* **2020**, *35*, 1113–1128. [CrossRef]
49. Kwon, Y.C.; Hong, S.Y. A Mass-Flux Cumulus Parameterization Scheme across Gray-Zone Resolutions. *Mon. Weather. Rev.* **2017**, *145*, 583–598. [CrossRef]
50. Hong, S.Y.; Lim, J.O.J. The WRF single-moment 6-class microphysics scheme (WSM6). *J. Korean Meteor. Soc.* **2006**, *42*, 129–151.
51. Jousse, A.; Hall, A.; Sun, F.; Teixeira, J. Causes of WRF surface energy fluxes biases in a stratocumulus region. *Clim. Dyn.* **2015**, *46*, 571–584. [CrossRef]
52. Dudhia, J. Numerical Study of Convection Observed during the Winter Monsoon Experiment Using a Mesoscale Two-Dimensional Model. *J. Atmos. Sci.* **1989**, *46*, 3077–3107. [CrossRef]
53. Mlawer, E.J.; Taubman, S.J.; Brown, P.D.; Iacono, M.J.; Clough, S.A. Radiative transfer for inhomogeneous atmospheres: RRTM, a validated correlated-k model for the longwave. *J. Geophys. Res. Atmos.* **1997**, *102*, 16663–16682. [CrossRef]
54. Hong, S.Y.; Noh, Y.; Dudhia, J. A new vertical diffusion package with an explicit treatment of entrainment processes. *Mon. Weather. Rev.* **2006**, *134*, 2318–2341. [CrossRef]
55. Jiménez, P.A.; Dudhia, J.; González-Rouco, J.F.; Navarro, J.; Montávez, J.P.; García-Bustamante, E. A Revised Scheme for the WRF Surface Layer Formulation. *Mon. Weather. Rev.* **2012**, *140*, 898–918. [CrossRef]
56. Mukul Tewari, N.; Tewari, M.; Chen, F.; Wang, W.; Dudhia, J.; LeMone, M.; Mitchell, K.; Ek, M.; Gayno, G.; Wegiel, J.; et al. Implementation and verification of the unified NOAH land surface model in the WRF model (Formerly Paper Number 17.5). In Proceedings of the 20th Conference on Weather Analysis and Forecasting/16th Conference on Numerical Weather Prediction, Seattle, WA, USA, 12–16 January 2004; Volume 14.
57. Renault, L.; Lemarié, F.; Arsouze, T. On the implementation and consequences of the oceanic currents feedback in ocean–atmosphere coupled models. *Ocean. Model.* **2019**, *141*, 101423. [CrossRef]
58. Tolman, H. Limiters in Third-Generation Wind Wave Models. *J. Atmos. Ocean. Sci.* **2002**, *8*, 67–83. [CrossRef]
59. Hasselmann, S.; Hasselmann, K. Computations and Parameterizations of the Nonlinear Energy Transfer in a Gravity-Wave Spectrum. Part I: A New Method for Efficient Computations of the Exact Nonlinear Transfer Integral. *J. Phys. Oceanogr.* **1985**, *15*, 1369–1377. [CrossRef]
60. Ardhuin, F.; Rogers, E.; Babanin, A.V.; Filipot, J.F.; Magne, R.; Roland, A.; van der Westhuysen, A.; Queffeulou, P.; Lefevre, J.M.; Aouf, L.; et al. Semiempirical Dissipation Source Functions for Ocean Waves. Part I: Definition, Calibration, and Validation. *J. Phys. Oceanogr.* **2010**, *40*, 1917–1941. [CrossRef]
61. Battjes, J.A.; Janssen, J.P.F.M. Energy Loss and Set-Up Due to Breaking of Random Waves. In *Coastal Engineering*; American Society of Civil Engineers: Reston, VA, USA, 1978. [CrossRef]
62. Ardhuin, F.; O'Reilly, W.C.; Herbers, T.H.C.; Jessen, P.F. Swell Transformation across the Continental Shelf. Part I: Attenuation and Directional Broadening. *J. Phys. Oceanogr.* **2003**, *33*, 1921–1939. [CrossRef]
63. Saha, S.; Moorthi, S.; Pan, H.L.; Wu, X.; Wang, J.; Nadiga, S.; Tripp, P.; Kistler, R.; Woollen, J.; Behringer, D.; et al. The NCEP Climate Forecast System Reanalysis. *Bull. Am. Meteorol. Soc.* **2010**, *91*, 1015–1058. [CrossRef]
64. Valcke, S. The OASIS3 coupler: A European climate modelling community software. *Geosci. Model Dev.* **2013**, *6*, 373–388. [CrossRef]
65. Pujol, M.I.; Faugère, Y.; Taburet, G.; Dupuy, S.; Pelloquin, C.; Ablain, M.; Picot, N. DUACS DT2014: The new multi-mission altimeter data set reprocessed over 20 years. *Ocean. Sci.* **2016**, *12*, 1067–1090. [CrossRef]
66. Bentamy, A.; Katsaros, K.B.; Drennan, W.M.; Forde, E.B. Daily Surface Wind Fields Produced by Merged Satellite Data. In *Geophysical Monograph Series*; American Geophysical Union: Washington, DC, USA, 2002; p. 343. [CrossRef]
67. Desbiolles, F.; Bentamy, A.; Blanke, B.; Roy, C.; Mestas-Nuñez, A.M.; Grodsky, S.A.; Herbette, S.; Cambon, G.; Maes, C. Two decades [1992–2012] of surface wind analyses based on satellite scatterometer observations. *J. Mar. Syst.* **2017**, *168*, 38–56. [CrossRef]
68. Aluie, H.; Hecht, M.; Vallis, G.K. Mapping the Energy Cascade in the North Atlantic Ocean: The Coarse-Graining Approach. *J. Phys. Oceanogr.* **2018**, *48*, 225–244. [CrossRef]
69. Leonard, A. Energy Cascade in Large-Eddy Simulations of Turbulent Fluid Flows. In *Turbulent Diffusion in Environmental Pollution, Proceedings of a Symposium held at Charlottesville*; Elsevier: Amsterdam, The Netherlands, 1975; pp. 237–248. [CrossRef]
70. Germano, M. Turbulence: The filtering approach. *J. Fluid Mech.* **1992**, *238*, 325–336. [CrossRef]

71. Schubert, R.; Gula, J.; Greatbatch, R.J.; Baschek, B.; Biastoch, A. The Submesoscale Kinetic Energy Cascade: Mesoscale Absorption of Submesoscale Mixed Layer Eddies and Frontal Downscale Fluxes. *J. Phys. Oceanogr.* **2020**, *50*, 2573–2589. [CrossRef]
72. Rai, S.; Hecht, M.; Maltrud, M.; Aluie, H. Scale of oceanic eddy killing by wind from global satellite observations. *Sci. Adv.* **2021**, *7*. [CrossRef]
73. Wazneh, H.; Gachon, P.; Laprise, R.; de Vernal, A.; Tremblay, B. Atmospheric blocking events in the North Atlantic: Trends and links to climate anomalies and teleconnections. *Clim. Dyn.* **2021**, *56*, 2199–2221. [CrossRef]
74. Kautz, L.A.; Martius, O.; Pfahl, S.; Pinto, J.G.; Ramos, A.M.; Sousa, P.M.; Woollings, T. Atmospheric blocking and weather extremes over the Euro-Atlantic sector – a review. *Weather. Clim. Dyn.* **2022**, *3*, 305–336. [CrossRef]
75. Renault, L.; Dewitte, B.; Falvey, M.; Garreaud, R.; Echevin, V.; Bonjean, F. Impact of atmospheric coastal jet off central Chile on sea surface temperature from satellite observations (2000–2007). *J. Geophys. Res. Ocean.* **2009**, *114*, 005083. [CrossRef]
76. Conejero, C.; Renault, L.; Desbiolles, F.; McWilliams, J.C.; Giordani, H. Near-Surface Atmospheric Response to Meso- and Submesoscale Current and Thermal Feedbacks. *J. Phys. Oceanogr.* **2024**, *54*, 823–848. [CrossRef]
77. Morrow, R.; Fu, L.L.; Ardhuin, F.; Benkiran, M.; Chapron, B.; Cosme, E.; d'Ovidio, F.; Farrar, J.T.; Gille, S.T.; Lapeyre, G.; et al. Global observations of fine-scale ocean surface topography with the Surface Water and Ocean Topography (SWOT) Mission. *Front. Mar. Sci.* **2019**, *6*, 1–19. [CrossRef]
78. Tréboutte, A.; Carli, E.; Ballarotta, M.; Carpentier, B.; Faugère, Y.; Dibarboure, G. KaRIn Noise Reduction Using a Convolutional Neural Network for the SWOT Ocean Products. *Remote Sens.* **2023**, *15*, 2183. [CrossRef]

Disclaimer/Publisher's Note: The statements, opinions and data contained in all publications are solely those of the individual author(s) and contributor(s) and not of MDPI and/or the editor(s). MDPI and/or the editor(s) disclaim responsibility for any injury to people or property resulting from any ideas, methods, instructions or products referred to in the content.